Low-friction study between diamond-like carbon coating and Ti 6Al 4V under fretting conditions

H.H. Ding, V. Fridrici, J. Geringer, Julien Fontaine, Ph Kapsa

Low-friction study between diamond-like carbon coating and Ti–6Al–4V under fretting conditions

H.H. Ding[1,3], V. Fridrici[1*], J. Geringer[2], J. Fontaine[1], Ph. Kapsa[1]

1. Laboratoire de Tribologie et Dynamique des Systèmes, UMR CNRS 5513 ECL-ENISE-ENTPE, Université de Lyon, Ecole Centrale de Lyon, Bat. TMM23, 36 avenue Guy de Collongue, 69134 Ecully cedex, France

2. Université de Lyon, IMT Mines Saint-Etienne, Centre CIS, INSERM, SainBioSE, F - 42023 Saint-Etienne, France

3. Tribology Research Institute, State Key Laboratory of Traction Power, Southwest Jiaotong University, Chengdu 610031, China

Abstract: Low friction between DLC coating and Ti–6Al–4V alloy was investigated under fretting conditions on a fretting-wear testing machine. The results indicated that, during the beginning period, the Ti–6Al–4V surface was damaged as a consequence of adhesion (and abrasion), leading to high friction coefficients of around 0.5. With the test ongoing, a tribofilm was formed on the rubbed Ti–6Al–4V surface. This tribofilm was derived from the wear product of Ti–6Al–4V alloy with oxidization. Its nano-hardness and reduced elastic modulus were greater than the Ti–6Al–4V matrix. Meanwhile, structural transformation occurred on the rubbed DLC surface. The tribofilm and transformed carbonaceous layer prevented the Ti–6Al–4V alloy and the DLC surface from direct contact and led to low friction coefficients (below 0.2).

Keywords: Low friction; Diamond-like carbon coating; Tribofilm; Roughness; Fretting

1. Introduction

In 1990s, modular neck adapters were introduced into hip-joint prostheses. The modular design facilitated the replacement surgery [1,2], but introduced a new contact, i.e., the neck adapter/femoral stem contact (Fig. 1 [3]). This new contact undergoes fretting damages when people walking [4,5]. In addition, Ti–6Al–4V alloy has been widely used for hip implants [6,7] including neck adapters and femoral stems [3]. But the Ti–6Al–4V/Ti–6Al–4V contacts exhibited large friction coefficients and adhesive damage under fretting situations [8,9].

DLC (diamond-like carbon) coatings were used to protect metallic components [10–12]. They exhibited excellent tribological properties owing to their low-friction and high-hardness in many environments [13,14]. Furthermore, DLC coatings showed high biocompatibility [15,16], which made it possible to be applied into implants. DLC coatings have already been introduced into hip implant at the femoral head/acetabular cup contact in clinic [17].

In our previous work [18], the fretting behavior of DLC coatings was studied in order to analyze their possible application at the Ti–6Al–4V neck adapter/Ti–6Al–4V femoral stem

*Corresponding author. Tel: +33 4 72 18 60 25.
E-mail address: vincent.fridrici@ec-lyon.fr (V. Fridrici).

contact. A cylinder-on-flat configuration was adopted to simulate the femoral stem-on-neck adapter contact. A DLC coating (labeled as "DLC A" in [18]) was deposited on the flat using the plasma-assisted chemical vapor deposition technique. Fretting tests were carried out under various values of displacement amplitude and normal force. According to the analysis of friction and coating damage, a coating response wear map was constructed (Fig. 2a). Under high load conditions, the DLC coating failed very soon after the fretting test started. The friction coefficient was high (around 0.6–1.0) throughout the entire test (red curve in Fig. 2b). Under low load conditions, the DLC coating functioned well throughout the entire test. The friction coefficient was high at the beginning, then decreased to low values (around 0.1–0.2) and then remained low and steady (green curve in Fig. 2b). In the present study, the aim is to explore the origin of low friction between the DLC coating and Ti–6Al–4V alloy under the low load condition.

Friction properties of DLC coatings have been studied under various experimental environments and shown to be sensitive to coating preparation, environmental conditions, etc. [19]. In general, a precondition for low friction is the absence of strong chemical bonds between the sliding surfaces. Three processes have a main contribution to the reduction of strong interfacial interaction during friction: (1) rehybridization with the structural transition of sp^3 to sp^2 on the rubbed DLC surface [20–22], induced by friction temperature [22] and/or by shear force [21]; (2) tribofilm formation on the rubbed countersurface [12,20,23,24]; and (3) passivation and repassivation of the DLC coating surface before and during sliding, i.e., dangling carbon bonds at the rubbed DLC surface chemically terminated by –H and/or –OH in active gases, such as hydrogen or water vapor [25,26].

Concerning the rehybridization and tribofilm formation processes, the low friction was achieved after the contact surfaces were changed during siding. Furthermore, from our previous work [18], for the DLC coating/Ti–6Al–4V contact under low load conditions, the low friction was achieved after the running-in period (green curve in Fig. 2b). This means that the contact surfaces were changed during the running-in period, and the changed contact surfaces led to the low friction. Therefore, in the present study, the first aim is to clarify which part of the contact (the rubbed DLC surface, or the rubbed Ti–6Al–4V surface, or both of them) is the key factor to the low friction. After that, the second aim is to explore the evolution of contact surfaces before, during, and after the running-in period. Tests will be conducted with different numbers of cycles, and both the rubbed DLC surface and rubbed Ti–6Al–4V surface will be analyzed with different analytical techniques. Based on friction coefficients and wear scars, a tribological model will be proposed for understanding the evolution of DLC coating/Ti–6Al–4V contact

during fretting.

2. Experimental details

2.1. Material characteristics

Flat and cylinder specimens were adopted to simulate the neck adapter and femoral stem, respectively. Both the flat and cylinder were made of the Ti–6Al–4V alloy. Concerning the surface roughness, two types of flats were studied: rough flat and smooth flat. For the cylinder, only a rough surface was adopted. A DLC coating was deposited on the flat samples using the PACVD technique with the machine TSD 550, from HEF [27]. The produced DLC coating was a-C:H with around 20 at.% of hydrogen.

2.1.1. Thickness of DLC coating

Fig. 3 shows the cross sections of DLC-coated flat specimens. The coating thickness reached around 2.0 μm. To improve the adhesion between the coating and the substrate, a Si-rich bonding layer was deposited on the Ti–6Al–4V surface.

2.1.2. Surface roughness

3D topographies of the real neck-adapter surface and the real femoral-stem inner surface are shown in Fig. 4. It is clear that the femoral-stem inner surface ($S_a \approx 475$ nm) was rougher than the neck-adapter surface ($S_a \approx 340$ nm). The sliding direction shown on the figures refers to the relative motions between neck-adapter and femoral-stem when people walking.

In the present study, the neck-adapter and femoral-stem components were simulated using a flat and a cylinder, respectively. Furthermore, in order to explore the effect of substrate roughness, two types of flats were used: smooth flat and rough flat. The rough flats and cylinders were machined to have similar roughness to the real neck-adapter and the real femoral-stem.

Fig. 5 shows the 3D topographies of flat and cylinder specimens. The sliding direction shown on the figures refers to the fretting direction for tests. The roughness (S_a) of flat and cylinder specimens is shown in Fig. 6. It is clear that the cylinder ($S_a > 700$ nm) was rougher than the rough flat ($S_a \approx 400$ nm). The smooth flat ($S_a \approx 20$ nm) was obviously smoother than the rough flat. Furthermore, the coating deposition has no obvious influence on the surface roughness.

2.1.3. Mechanical properties of DLC coating and Ti–6Al–4V substrate

To measure the hardness and reduced elastic modulus, nano-indentation tests were

performed on the DLC-coated smooth flat and on the uncoated Ti–6Al–4V flat, using a nano-indenter (Nano Indenter XP, MTS) with the continuous stiffness measurement mode. On each sample, the measurement was conducted nine times at different spots. The maximal indentation load was 450 mN. Fig. 7 shows the results of nano-indentation tests. On the Ti–6Al–4V flat, the nano-hardness was around 3.4 GPa. The reduced elastic modulus was around 122 GPa. On the DLC-coated flat, the nano-hardness and reduced elastic modulus were greater. The nano-hardness was around 29 GPa at the penetration depth of 50–200 nm. With the increase in the penetration depth, the nano-hardness significantly decreased. The reduced elastic modulus was around 236 GPa at the penetration depth of 50–150 nm.

2.2. Fretting test machine and samples

Tests were carried out on a fretting-wear machine with a flat/cylinder contact, as shown in Fig. 8a. The normal force was applied between the flat and the cylinder. The flat was moved up and down by a given controlled displacement, and the cylinder was fixed. During the test, the normal forces, the displacement amplitudes, and the tangential forces were recorded, which enabled us to calculate friction coefficients and plot fretting logs [28]. Fig. 8b shows the geometry of the flat and cylinder specimens. The diameter and length of cylinder were 20 mm and 5 mm, respectively.

2.3. Test conditions

According to the results of finite element modeling of the real parts in previous works [4,5], the maximum contact pressure between the neck adapter and the femoral stem was in the range of 280-690 MPa and the relative motion was in the range of 3-41 µm during the patient walking. Thus, in the present fretting tests, the normal force of 250 N was adopted (leading to the maximum contact pressure of 316 MPa) and the displacement was ±20 µm. Besides the fact that the average frequency of human walking is around 1 Hz, in this study, the frequency was fixed at 5 Hz, to achieve a large number of cycles in a relatively short test time period. Thus, the average sliding speed was around 6-82 µm/s in the patient's body while it was 200 µm/s in the fretting tests. The effects of normal force (i.e., the contact pressure) and the displacement (i.e., the sliding speed) on the fretting behaviors between neck adapter and femoral stem were studied in our previous work [29].

In the patient's body, the hip implant works at the temperature of around 37°C and is surrounded by the synovial fluid. In the present study, fretting tests were performed in the laboratory air condition. Humidity and temperature cannot be controlled, but were recorded and ranged from 30 % to 50 % and 18°C to 23°C, respectively. The influence of the synovial fluid

on the fretting behaviors between neck adapter and femoral stem was investigated in our previous work [30]. After fretting tests, many surface analysis techniques were used including an interferometer, optical microscope, scanning electron microscope (SEM), nano-indentation tests, and Raman spectrometer. Cross sections were cut parallel to the sliding direction, ground to 4000 grit, polished to 1-μm diamond, and then observed using SEM.

3. Results

3.1. Friction coefficient and slip regime

In this study, all the fretting tests were in the gross slip regime (GSR). The friction coefficient μ was defined as Q_{max}/P, where Q_{max} was the maximal tangential force during a fretting cycle; P was the corresponding normal force. The evolution of μ and the fretting logs for rough and smooth flats with and without DLC coating are shown in Fig.9. The energy ratio A (dissipated energy divided by total energy of a cycle) was used to classify the slip regimes [28]. In general, the fretting was in the GSR if the value of A was larger than 0.2 [31]. The A values shown in Fig. 9 are the average values obtained during the entire test.

For the Ti–6Al–4V/Ti–6Al–4V contact, the fretting was in the GSR (Figs. 9b,c). The value of A were around 0.55 and 0.57 on a rough flat and on a smooth flat, respectively. Concerning the friction coefficient μ (Fig. 9a), it increased to a high value of approximately 1.1 during the first approximately 200 cycles, and then remained high until the end of the test. The roughness had no significant influence on the μ.

For the DLC coating/Ti–6Al–4V contact, the fretting was also in the GSR (Figs. 9d,e). The values of A were around 0.50 and 0.62 for tests on a DLC coated rough flat and on a DLC coated smooth flat, respectively. Concerning the friction coefficient μ, it showed an increase during the first 10 cycles. This was because the displacement amplitude of the flat increased gradually from 0 to the set value during the first 10 cycles (i.e., the ramping-in period). After that, the μ decreased rapidly to a low value during approximately 100 cycles (i.e., the running-in period), and then remained steady until the completion. The roughness had an influence on μ. In the running-in period, the maximal value of μ on the rough flat was higher than that on the smooth flat. In the steady state, the friction coefficient of the rough flat was slightly higher than that of the smooth flat. Furthermore, during the steady state, the friction coefficient for the rough flat showed a slight decrease from 0.18 to 0.13, whereas, for the smooth flat, the friction coefficient was approximately 0.11 and showed no obvious decrease.

3.2. Friction coefficient under different contact conditions

It is clear from Section 3.1 that the friction coefficient μ of the DLC coating/Ti–6Al–4V contact decreased to a low value after 100 cycles. To clarify which part of the contact surfaces (the rubbed DLC coating surface, the rubbed Ti–6Al–4V surface, or both of them) led to the low friction, three different series of tests were conducted (Fig. 10). Fig. 11 shows the evolution of μ.

In series 1 (the black dotted curves in Fig. 11), after 100 cycles (i.e., the running-in period), the test was stopped, and then restarted for another 100 cycles. A continuous low friction coefficient was obtained except for the first 10 cycles (between cycles 101 and 110), because of the ramping-in period.

At cycle 200, the test was stopped. The flat/cylinder contact was opened and then put again into contact. The normal force was applied again, and the test was restarted for another 100 cycles. These processes were repeated at cycle 300. As shown by the black dotted curves from cycles 201 to 400 in Fig. 11, putting into contact the already-rubbed Ti–6Al–4V surface (cylinder) with the already-rubbed DLC coating (flat) resulted in a new small running-in period because of the change in the pressure distribution when reloaded. Compared to the running-in period from cycle 1 to 100, this new small running-in period had a much lower μ. Specifically, the maximal value of μ during the test from cycles 201 to 300 was 0.3 on the rough flat (Fig. 11a). It was lower (0.18) on the smooth flat (Fig. 11b).

In series 2 (the red solid curves in Fig. 11), after 100 cycles, the test was stopped, and the flat/cylinder contact was opened. And then, the cylinder was rotated to present a new Ti–6Al–4V surface for the contact with the already-rubbed DLC coating surface. The normal force was applied again, and the test was restarted for another 100 cycles. These processes were repeated three times.

As shown by the red solid curves in Fig. 11, putting into contact a new Ti–6Al–4V surface (cylinder) with the already-rubbed DLC coating (flat) led to a new running-in period. Furthermore, this new running-in period was almost identical to the one from the test with the new Ti–6Al–4V surface in contact with the new DLC coating (i.e., from cycle 1 to 100). In other words, as soon as a new Ti–6Al–4V surface came into contact, a 100-cycles running-in period was necessary to cause a reduction in the μ. Moreover, on the DLC coated rough flat, the maximal value of μ was approximately 0.65 during each 100 cycles (Fig. 11a). On the DLC coated smooth flat, the maximal value of μ was lower (approximately 0.45, as shown in Fig. 11b), as expected.

In series 3 (the green fine curves in Fig. 11), after 100 cycles, the test was stopped, and the flat/cylinder contact was opened. And then, the flat was moved to present a new DLC

coating surface for the contact with the already-rubbed Ti–6Al–4V surface. The normal force was applied again, and the test was restarted for another 100 cycles. These processes were repeated three times.

As shown by the green fine curves in Fig. 11, putting into contact a new DLC coating surface (flat) with the already-rubbed Ti–6Al–4V surface (cylinder) led to a new small running-in period, which was similar to the small running-in period of the test in series 1 from cycles 201 to 300 (i.e., the already-rubbed Ti–6Al–4V surface in contact with the already-rubbed DLC coating).

The relationship between the friction and the contact condition is shown in Table 1. It can be concluded that the friction was closely dependent on the state of Ti–6Al–4V surface. Specifically, a new Ti–6Al–4V surface always caused high friction, and a rubbed Ti–6Al–4V surface always caused low friction. The state of DLC coating surface (new or rubbed) had no obvious influence on the friction coefficient (high or low).

3.3. Evolution of wear scars

From section 3.2, it is clear that the rubbed Ti–6Al–4V surface after the running-in period was the key factor for low friction. For better understanding tribological behaviors of the DLC coating/Ti–6Al–4V contact, the evolution of contact surfaces was explored. Tests were carried out with different numbers of cycles: 0 (maintaining the surfaces in contact for 10 s, then opening the contact), 1, 20, 40, 100 (just after the running-in period), and 100 000 cycles on the DLC coated rough flat. On the DLC coated smooth flat, tests were carried out with 0, 1, 100, and 100 000 cycles. The normal load (250 N) and displacement (±20 μm) were the same to tests in section 3.2. After that, wear scars on both Ti–6Al–4V and DLC coating surfaces were observed and analyzed in detail.

3.3.1. Contact only (0 fretting cycle)

The DLC coating (flat) and Ti–6Al–4V (cylinder) surfaces were put into contact for 10 s, and then the contact was opened.

- **Rough flat/rough cylinder**

The Ti–6Al–4V and rough DLC coating surfaces are shown in Fig. 12 and Fig. 13, respectively. Obviously, some Ti–6Al–4V was removed and scratches were observed on the cylinder surface (Fig. 12). On the DLC coating surface, some material was adhered (Fig. 13). From the analysis of EDX, this adhered material was composed of titanium, aluminum, and vanadium, thus suggesting that the Ti-alloy was transferred to the DLC surface. There were two

possibilities leading to this transfer: (1) adhesion between the DLC coating and the Ti alloy; and (2) abrasion of the rough hard DLC surface on the soft Ti-alloy. For abrasion processes, relative motion was required. It might be derived from the elastic and plastic deformation of samples under the normal force, and/or from the roughness of the samples. In addition, No obvious oxygen was detected in the transferred material. Furthermore, no obvious carbon element was detected on the Ti–6Al–4V surface.

- **Smooth flat/rough cylinder**

For the test on the DLC coated smooth flat, the Ti–6Al–4V and coating surfaces are shown in Fig. 14 and Fig. 15, respectively. It is clear from Fig. 14 that less Ti–6Al–4V was removed from the cylinder, and the damage on the cylinder surface was milder when it was in contact with the smooth flat than in contact with the rough flat (Fig. 12). Accordingly, less Ti-alloy was adhered on the smooth DLC coating surface (Fig. 15).

Because of the smoothness of the smooth DLC coating surface, the abrasion process could be negligible. Therefore, the Ti–6Al–4V transfer from cylinder to the smooth flat was mainly derived from the adhesion process. It can also be concluded that the adhesion did occur between the DLC surface and the Ti–6Al–4V surface before the friction started.

3.3.2. After 1 cycle

- **Rough flat/rough cylinder**

Fig.16 shows the Ti–6Al–4V surface and rough DLC coating surface after 1 cycle. Compared to the test before sliding (Fig. 12 and Fig. 13), the damage on the cylinder surface was more severe with obvious scratches parallel to the fretting direction. And much more Ti-alloy was transferred to the rough DLC coating surface (Fig. 16b), this is because the sliding motion significantly enhanced the abrasion processes of the rough DLC coating.

- **Smooth flat/rough cylinder**

Fig. 17 shows the Ti–6Al–4V surface and smooth DLC coating surface after 1 cycle. Compared to the test before sliding (Fig. 14 and Fig. 15), the damage on the Ti–6Al–4V cylinder surface was slightly more severe with scratches (Fig. 17a). Slightly more Ti-alloy was adhered to the DLC coating surface (Fig. 17b). This is because the sliding motion slightly enhanced the adhesion processes of the smooth DLC coating. Compared to the test on a rough flat after 1 cycle (Fig. 16), the damage of the Ti–6Al–4V surface was much milder. Much less Ti-alloy was adhered to the smooth DLC coating surface.

In summary, at the beginning of testing, Ti–6Al–4V was worn off from the cylinder as a consequence of adhesion (when against a smooth DLC coating) or as a consequence of both

adhesion and abrasion (when against a rough DLC coating). Energy was needed to break the metallic bonds in the Ti–6Al–4V side. The dissipated energy during each cycle was an integral of displacement and friction force. Therefore, the friction was high at the beginning of the test (Fig. 9).

In addition, more Ti–6Al–4V was worn off when sliding against a DLC coated rough flat than against a DLC coated smooth flat. Therefore, the friction was higher on a rough DLC coating surface than on a smooth DLC coating surface at the beginning of the test (Fig. 9a).

3.3.3. After 20 cycles (in running-in)

- **Rough flat/rough cylinder**

Fig.18 shows the Ti–6Al–4V surface after 20 cycles (i.e. in the running-in period, when the friction coefficient was high). Obviously, the worn-off material was pressed in the contact, forming a tribofilm on the rubbed Ti–6Al–4V surface (Figs. 18c,d). The tribofilm was composed of titanium, aluminum, vanadium, and a quantity of oxygen (Fig. 18e), suggesting that the tribofilm was derived from the worn-off Ti-alloy with severe oxidation due to the repeated sliding in air. Furthermore, cracks were generated in the tribofilm perpendicularly to the sliding direction because of the repeated sliding and the stress variation (Fig. 18d). In addition, some DLC particles were observed on the tribofilm surface (Figs. 18f,g).

Fig.19 shows the rough DLC coating surface after 20 cycles. Compared to the flat surface after 1 cycle (Fig. 16b), much less Ti-alloy was adhered on the coating surface (Fig. 19b). From the analysis of EDX (Fig. 19e), this adhered material was composed of titanium, aluminium and vanadium. No visible oxygen was detected. This suggests that the adhered material was derived from the Ti transfer, not from the tribofilm material. Some of the original adhered material was worn off with the test ongoing. In addition, a small part of coating was detached (Fig. 19c). That is why DLC particles were observed on the countersurface (Figs. 18f,g).

3.3.4. After 40 cycles (in running-in)

- **Rough flat/rough cylinder**

Fig. 20 shows the Ti–6Al–4V surface after 40 cycles. With the test ongoing from 20 cycles to 40 cycles, more tribofilm material was formed and the rubbed area was almost totally covered by the tribofilm (Figs. 20b,c). The friction coefficient decreased to around 0.49 (Fig. 11a). Fig. 21 shows the corresponding DLC coating surface. Less Ti-alloy was adhered on the DLC surface (Fig. 21b). Besides, the DLC coating was also detached (Fig. 21c) and DLC particles were also observed on the cylinder surface (Figs. 20d,e).

3.3.5. After 100 cycles (just after running-in)

- **Rough flat/rough cylinder**

Fig. 22 shows the Ti–6Al–4V surface after 100 cycles (just after the running-in period). With the test ongoing from 40 cycles to 100 cycles, more Ti–6Al–4V surface went into contact due to wear. More tribofilm material was formed (Fig. 22b). The friction coefficient decreased from around 0.49 to around 0.2 (Fig. 11a). Besides, the tribofilm was also oxidized, and cracks (Fig. 22c) and DLC particles (Figs. 22d,e) were also observed on the tribofilm surface.

Fig. 23 shows the rough DLC coating surface after 100 cycles (just after the running-in). With the testing ongoing from 40 cycles to 100 cycles, much less adhered Ti-alloy was observed (Figs. 23a,b,c). The formed tribofilm prevented the coating and Ti–6Al–4V surfaces from direct contact, obstructing the transfer of Ti-alloy.

Furthermore, scratches were observed on the DLC surface (Fig. 23c), indicating that the DLC material could be worn off. Moreover, cracks were generated on the coated rough flat (Figs. 23d,e). Some pieces of coating were flaked off (Fig. 23e) and transferred to the countersurface (Figs. 22d,e) and/or might be ejected as debris.

- **Smooth flat/rough cylinder**

Fig. 24 shows the Ti–6Al–4V surface (against the DLC coated smooth flat) after 100 cycles. A tribofilm was formed and it was oxidized. Furthermore, EDX analysis seems to indicate the presence of a “thin carbonaceous layer” on the tribofilm surface (Figs. 24b,c,d). The darker the area on the SEM image was, the higher content of carbon was detected by EDX. Besides, the “thin carbonaceous layer” was also observed on the trbofilm surface when it was in contact with a DLC coated rough flat (Fig. 22e). In addition, there were no cracks formed on the tribofilm, which is probably due to the smoothness of the smooth DLC coating surface.

Fig. 25 shows the smooth DLC coating surface after 100 cycles. It is noteworthy that the DLC coating was not fractured. Correspondingly, no DLC particles were observed on the Ti–6Al–4V countersurface (Fig. 24). Besides, some Ti-alloy was still adhered on the DLC coating surface.

3.3.6. After 100 000 cycles

- **Rough flat/rough cylinder**

Fig. 26 shows the Ti–6Al–4V surface and the rough DLC coating surface after 100 000 cycles. Compared to the Ti–6Al–4V surface after 100 cycles (Figs. 22a,b), slightly more tribofilm material was formed on the cylinder (Figs. 26a,c). Therefore, the friction coefficient decreased slightly from around 0.2 to around 0.13 between 100 and 100 000 cycles (Fig. 9a).

Furthermore, the cracks on the DLC coating (Figs. 23d,e) were developed into pits (Fig. 26d) where the coating was removed. Meanwhile, no Ti-alloy was adhered on the DLC coating surface.

- **Smooth flat/rough cylinder**

Fig. 27 shows the Ti–6Al–4V surface and the smooth DLC coating surface after 100 000 cycles. The tribofilm was similar to the tribofilm after 100 cycles (Fig. 24a); i.e., no more tribofilm material was formed on the cylinder. Therefore, the friction coefficient showed no change in the steady state between 100 and 100 000 cycles (Fig. 9a). On the DLC coating surface, no cracks were generated; i.e., the DLC coating on the smooth flat did not break until 100 000 cycles. Meanwhile, no Ti-alloy was adhered on the DLC coating surface.

It is clear that, in the low friction period, the tribofilm (and the carbonaceous layer) prevented the Ti–6Al–4V and DLC coating surfaces from direct contact. Meanwhile, neither Ti–6Al–4V nor tribofilm was transferred from the Ti side to the coating side, which reveals that the adhesive force between the DLC surface and the tribofilm surface was lower than the cohesive forces in the cylinder side (i.e., the cohesive force inside the tribofilm, the cohesive force inside the Ti-alloy, and the bonding force between the tribofilm and Ti-alloy). Thus, the dissipated energy at the interface was low, and the friction coefficient was low.

3.4. Properties of rubbed contact surfaces

From section 3.3, for the DLC coating/Ti–6Al–4V contact in fretting, a tribofilm and a thin carbonaceous layer were formed on the rubbed Ti–6Al–4V cylinder. To facilitate the measurement of properties of the tribofilm and carbonaceous layer, they were produced on a Ti–6Al–4V flat surface through fretting testing with an uncoated rough flat/DLC coated cylinder contact for 100 000 cycles. Analysis on a flat surface was easier to perform than on a cylindrical surface. The friction coefficient evolution was similar for uncoated flat/DLC coated cylinder contact and for DLC coated flat/uncoated cylinder contact.

3.4.1. Thickness of tribofilm

The cross sections of the rubbed Ti–6Al–4V flat were cut, polished, and then observed using the SEM with an observation angle of 6° (Fig. 28). The tribofilm thickness reached approximately 0.7 μm in the central area of contact (Fig. 28a). The tribofilm material heaped up in the valley on the border area of the contact, leading to the maximal thickness of approximately 2 μm (Fig. 28b).

3.4.2. Mechanical properties of tribofilm

Nano-hardness and reduced elastic modulus were measured on the tribofilm and the substrate. The measurement was repeated nine times at different positions. The maximal indentation load was 100 mN. Fig. 29 shows representative indents.

Fig. 30 shows the nano-hardness and reduced elastic modulus as a function of the plastic penetration depth. On the Ti–6Al–4V substrate, the nano-hardness was approximately 3.9 GPa. The reduced elastic modulus was approximately 130 GPa. On the tribofilm, the nano-hardness and reduced elastic modulus were higher. The nano-hardness was approximately 10 GPa at the penetration depth of 60–120 nm, which was approximately 2.6 times higher than the nano-hardness of the substrate. The reduced elastic modulus was approximately 170 GPa at the penetration depth of 60–120 nm, which was 1.3 times higher than that of the substrate.

Besides, it is noteworthy that the work-hardening of Ti–6Al–4V surface might have a contribution to the high hardness measured on the tribofilm. From the etched cross section (as shown in Fig. 31), the microstructure of substrate beneath the tribofilm showed no obvious difference with that outside the contact, which suggests that the contribution of work-hardening on the substrate surface might be negligible.

3.4.3. Raman spectroscopy on rubbed surfaces

Raman spectroscopy consists of measuring the intensity of inelastically scattered light as a function of the wavelength [32]. It is an interesting, non-destructive tool for structural characterisation of carbon [33]. Raman spectroscopic measurements were performed on the unworn DLC surface (on a smooth flat), worn DLC surface (on a smooth flat), tribofilm surface (formed on a rough flat), and unworn Ti–6Al–4V surface (a smooth flat) using a Raman spectrometer (XploRA, HORIBA Scientific). The laser with wavelength of 785 nm and power of 35 mW was adopted. All Raman spectra were recorded with a 600 lines/mm grating. Three measurements were performed at different spots on each surface, and they showed very similar spectra. Fig. 32 shows the Raman spectra on the unworn DLC, worn DLC, tribofilm, and Ti–6Al–4V surfaces.

According to pervious works, the Raman spectra of DLC consist of G and D peaks [33]. The G peak corresponds to the bond stretching of all pairs of sp^2 atoms in both rings and chains. D_1 and D_2 peaks correspond to breathing modes of sp^2 atoms in rings. The Gaussian fit was used in this study to fit the Raman spectra in order to extract typical characteristics, such as the positions and intensities of peaks.

Fig. 33 shows Gaussian fitting of the Raman spectra on the unworn DLC surface, the worn DLC surface, and the tribofilm surface. A careful analysis of the G peak position and the ratio

of intensities of D and G peaks ($I(D_1+D_2)/I(G)$) could provide information about the structural transformation on DLC surface. The fitting results are shown in Table 2.

The unworn DLC surface (outside the contact area) exhibited a typical spectrum of a-C:H with dominant peaks (G and D_1) and a wide shoulder caused by a small D_2 peak at low wavenumbers [34]. The G and D_1 lay at around 1500 cm^{-1} and 1300 cm^{-1}, respectively. The $(I(D_1+D_2)/I(G))$ was around 2.04.

The spectrum acquired on the worn DLC surface (inside wear track) exhibited clear differences compared to that on the unworn DLC surface, as shown in Fig. 32. The G peak shifted towards lower wavenumbers, which means a higher level of order in the carbon amorphous network [32]. The $I(D_1+D_2)/I(G)$ increased to around 2.55, suggesting an increase in size of sp^2 ring-like carbon clusters [32,33]. In addition, a peak was detected at around 930 cm^{-1}, which might probably be due to some oxidization processes. The difference Raman spectra inside and outside the wear track on the DLC surface revealed that a structural transformation occurred on the DLC surface during sliding.

The Raman spectrum acquired on the tribofilm surface was similar to that on the worn DLC surface, such as the similar positions of peaks, and high values of $I(D_1+D_2)/I(G)$, but with a lower photoluminescence background intensity (Fig. 32). This means that the transformed material on the worn DLC surface was transferred to the countersurface. This corresponds to the "carbonaceous layer" observed via SEM and EDX on the tribofilm surface (Fig. 24).

It can be concluded that structural transformation occurred on the rubbed DLC surface during sliding. And the transformed carbonaceous material was transferred to the counterbody. Therefore, the rubbed DLC/rubbed Ti–6Al–4V contact was "DLC coating + carbonaceous layer"/"carbonaceous layer + tribofilm + Ti–6Al–4V" contact. Further exploration could be performed to investigate the nature of the carbonaceous layer in the future.

4. Discussion

4.1. Analysis of origin of low friction

For the DLC coating/Ti–6Al–4V contact in fretting, after the running-in period, a tribofilm was formed on the rubbed Ti–6Al–4V surface. The tribofilm had higher nano-hardness and higher reduced elastic modulus than the Ti–6Al–4V alloy. On the rubbed DLC surface, structural transformation occurred. And the transformed material was transferred to the countersurface. Thus, the rubbed DLC coating/rubbed Ti–6Al–4V contact situation was "DLC coating + carbonaceous layer"/"carbonaceous layer + tribofilm + Ti–6Al–4V".

In addition, a fretting test with a DLC coating/DLC coating contact (i.e., DLC coated rough

flat/DLC coated rough cylinder) was conducted for 100 000 cycles. Fig. 34 shows the evolution of μ (green curve). It remained low during the entire test. At the beginning of the test, the contact situation was "DLC coating"/"DLC coating" and the μ was around 0.20. After that, the friction coefficient showed a slight increase to around 0.26, which was probably due to the break of DLC particles on the rough surfaces. With the test ongoing, the DLC surfaces became smooth, and a carbonaceous layer was formed on the rubbed DLC surface. The contact situation was "DLC coating + carbonaceous layer"/"carbonaceous layer + DLC coating" and the friction coefficient was around 0.17.

The relationship between the friction and the contact situations is shown in Table 3. Obviously, the friction was closely dependent on properties of the countersurface. However, the DLC surface state (new DLC or rubbed DLC) had no obvious influence on the friction.

When the countersurface was new Ti–6Al–4V (#1 and #3), the friction was high. This is because the soft Ti–6Al–4V was easy to be damaged, as a consequence of adhesion and abrasion. The energy needed to break the metallic bonds in the Ti–6Al–4V side led to high friction. In the case of #3, a carbonaceous layer was present at the interface. However, the presence of carbonaceous layer cannot lead to the low friction between DLC coating and new Ti–6Al–4V surfaces.

When the countersurface was rubbed Ti–6Al–4V (i.e., carbonaceous layer + tribofilm, #2 and #4), the friction was low. The low friction was probably due to the high hardness and high elasticity of the tribofilm material. Whether the presence of carbonaceous layer on the tribofilm surface was required to the low friction was uncertain.

When the countersurface was another DLC coating (with high hardness and high elasticity, #5 and #6), the friction was low. Comparing #6 with #5, the presence of carbonaceous layer between two DLC coating surfaces had no important influence on the low friction.

Therefore, it can be concluded that for the DLC coating/Ti–6Al–4V contact in fretting, the low friction was closely related to the presence of tribofilm on the rubbed Ti–6Al–4V surface (#2 and #4). The relation between the presence of carbonaceous layer and the low friction state was unclear. At least, the carbonaceous layer itself cannot lead to low friction between DLC and Ti–6Al–4V (#3).

4.2. Tribological model for the evolution of DLC coating/Ti–6Al–4V contact

Based on analysis of friction coefficients and wear scars, a tribological model was proposed to explain the tribological behaviors of DLC coating/Ti–6Al–4V contact in fretting (Fig. 35). The evolution of friction can be divided into three periods: high-friction period,

friction-decreasing period, and low-friction period.

- **High-friction period**

At the beginning of fretting, Ti–6Al–4V surface was worn off as a consequence of adhesion (and abrasion). Some Ti-alloy was transferred to the DLC coating surface. The energy needed to break the metallic bonds in the Ti–6Al–4V side led to high friction coefficients.

In addition, the sliding enhanced the abrasion effect of the hard rough DLC surface on the soft Ti–6Al–4V alloy. Therefore, when the cylinder slid against the DLC coated rough flat, more Ti–6Al–4V was worn off and a higher friction coefficient was obtained.

- **Friction-decreasing period**

The worn-off Ti–6Al–4V was pressed repeatedly at the interface and was oxidized in air. With the test ongoing, the worn-off Ti–6Al–4V material formed a tribofilm on the rubbed Ti–6Al–4V surface. The tribofilm had higher nano-hardness and higher reduced elastic modulus than the Ti–6Al–4V substrate. Meanwhile, the structural transformation occurred on the rubbed DLC surface. And the transformed carbonaceous material was transferred to the counterbody, forming a carbonaceous layer on the tribofilm surface.

- **Low-friction period**

A functional tribofilm was achieved after the running-in period, and a thin carbonaceous layer was present on the tribofilm surface and on the rubbed DLC surface. The tribofilm and carbonaceous layer prevented the DLC coating and Ti–6Al–4V from direct contact. The material transfer from the Ti–6Al–4V side to the DLC coating surface was obstructed. The adhesive force between the coating and the tribofilm was low, and the friction coefficient was low.

In addition, during the running-in period, the DLC coating on the rough flat was broken, due to the high local contact pressure between asperities from both contacting surfaces. With the test ongoing for a long time (100 000 cycles), the cracks of the DLC coating developed into pits. However, the DLC coating deposited on the smooth flat did not break until 100 000 cycles.

The modular design of the hip implant with the neck adapter was a new design aiming to facilitate the surgery operation. The application of DLC coating into the neck adapter/femoral stem contact was also a new idea to protect the Ti-alloy substrate. According to the results of this study, the DLC coating could reduce friction and protect the Ti-6Al-4V substrate. However, the fretting tests were performed in the laboratory air condition; *in vivo* experiments should then be conducted to explore whether the new product is suitable to the patient therapy. Our previous study showed that the presence of serum liquid showed no adverse effects on tribological performances of this DLC coating [30]. However, the effects of passivation of DLC surface and

body temperature on the performance of the hip implant could be explored in the future.

5. Conclusions

Fretting tests were performed between a DLC coating and the Ti–6Al–4V alloy. Based on the analysis of friction coefficients and wear scars, the following conclusions can be drawn:

(1) For the DLC coating/Ti–6Al–4V contact, friction coefficients were high (around 0.5) at the beginning of fretting test. After that, it decreased to low values (below 0.2) during the first 100 cycles (i.e., the running-in period).

(2) After the running-in period, the new Ti–6Al–4V surface/already-rubbed DLC coating surface contact led to a high friction coefficient (i.e., a new running-in period), which was the same as the new Ti–6Al–4V surface/new DLC coating surface contact. However, the new DLC coating surface/already-rubbed Ti–6Al–4V surface contact resulted in a low friction coefficient, which was similar to the rubbed Ti–6Al–4V surface/rubbed DLC coating surface contact. Therefore, the rubbed Ti–6Al–4V surface was the key factor to the low friction.

(3) At the beginning of fretting test, the Ti–6Al–4V surface was in direct contact with the DLC coating surface. The Ti–6Al–4V surface was damaged as a consequence of adhesion (and abrasion), leading to the high friction.

(4) During the running-in period, a tribofilm was gradually formed on the rubbed Ti–6Al–4V surface. This tribofilm was derived from worn-off Ti alloy with severe oxidization. The thickness was around 0.7–2 μm after 100 000 cycles. The nano-hardness on the tribofilm was 2.7 times higher and the elastic modulus was 1.3 times higher than those on the Ti–6Al–4V substrate. Structural transformation occurred on the rubbed DLC surface, and the transformed material was transferred to the counterbody, forming a carbonaceous layer on the tribofilm surface. The tribofilm and carbonaceous layer separated the Ti–6Al–4V and the DLC coating from direct contact and led to the low friction after the running-in period.

(5) The surface roughness had effects on the friction and surface damage. The rougher DLC coating surface led to a slightly higher friction coefficient. The DLC coating deposited on the rough flat was broken before 100 cycles; however, on the smooth flat, it was not broken until the end of the test (100 000 cycles).

Acknowledgement

The authors would like to thank LABEX MANUTECH-SISE (ANR-10-LABX-0075) of Université de Lyon, within the program "Investissements d'Avenir" (ANR-11-IDEX-0007)

operated by the French National Research Agency (ANR), for its support. The authors also would like to thank the China Scholarship Council for its support.

References

[1] Gofton WT, Illical EM, Feibel RJ, Kim PR, Beaulé PE. A single-center experience with a titanium modular neck total hip arthroplasty. J Arthroplasty 2017;32:2450–2456. https://doi.org/10.1016/j.arth.2017.03.025

[2] Grupp TM, Weik T, Bloemer W, Knaebel H. Modular titanium alloy neck adapter failures in hip replacement - failure mode analysis and influence of implant material. BMC Musculoskeletal Disorders 2010;11:3. https://doi.org/10.1186/1471-2474-11-3

[3] XO modular femoral stem from the company SEM *Science et Médecine* in France. http://www.aston-sem.com/professional-space/hip/?lang=en#1510161431587-49af8836-f910

[4] Jauch SY, Huber G, Haschke H, Sellenschloh K, Morlock MM. Design parameters and the material coupling are decisive for the micromotion magnitude at the stem–neck interface of bi-modular hip implants. Med Eng Phys 2014;36:300–307. https://doi.org/10.1016/j.medengphy.2013.11.009

[5] Baxmann M, Jauch SY, Schilling C, Blömer W, Grupp TM, Morlock MM. The influence of contact conditions and micromotions on the fretting behavior of modular titanium alloy taper connections. Med Eng Phys 2013;35:676–683. https://doi.org/10.1016/j.medengphy.2012.07.013

[6] Kunčická L, Kocich R, Lowe TC. Advances in metals and alloys for joint replacement. Prog Mater Sci 2017;88:232–280. https://doi.org/10.1016/j.pmatsci.2017.04.002

[7] Chen Q, Thouas GA. Metallic implant biomaterials. Mater Sci Eng R 2015;87:1–57. https://doi.org/10.1016/j.mser.2014.10.001

[8] Fridrici V, Fouvry S, Kapsa Ph. Effect of shot peening on the fretting wear of Ti–6Al–4V. Wear 2001;250:642–649. https://doi.org/10.1016/S0043-1648(01)00671-8

[9] Van Peteghem B, Fouvry S, Petit J. Effect of variable normal force and frequency on fretting wear response of Ti–6Al–4V contact. Wear 2011;271:1535–1542. https://doi.org/10.1016/j.wear.2011.01.060

[10] Bewilogua K, Hofmann D. History of diamond-like carbon films—From first experiments to worldwide applications. Surf Coat Technol 2014;242:214–225. https://doi.org/10.1016/j.surfcoat.2014.01.031

[11] Grill A. Tribology of diamond like carbon and related materials: an updated review. Surf Coat Technol 1997;94–95:507–513. https://doi.org/10.1016/S0257-8972(97)00458-1

[12] Hauert R. An overview on the tribological behavior of diamond-like carbon in technical and medical applications. Tribol Int 2004;37:991–1003. https://doi.org/10.1016/j.triboint.2004.07.017

[13] Grill A. Diamond-like carbon: state of the art. Diam Relat Mater 1999;8:428–434. https://doi.org/10.1016/S0925-9635(98)00262-3

[14] Grill A. Review of the tribology of diamond-like carbon. Wear 1993;168:143–153. https://doi.org/10.1016/0043-1648(93)90210-D

[15] Thomson LA, Law FC, Rushton N, Franks J. Biocompatibility of diamond-like carbon coating. Biomaterials 1991;12:37–40. https://doi.org/10.1016/0142-9612(91)90129-X

[16] Allen M, Myer B, Rushton N. *In vitro* and *in vivo* investigations into the biocompatibility of diamond-like carbon (DLC) coatings for orthopedic applications. J Biomed Mater Res 2001;58:319–328. https://doi.org/10.1002/1097-4636(2001)58:3<319::AID-JBM1024>3.0.CO;2-F

[17] Taeger G, Podleska LE, Schmidt B, Ziegler M, Nast-Kolb D. Comparison of diamond-like-carbon and alumina-oxide articulating with polyethylene in total hip arthroplasty. Mater Sci Eng Technol 2003;34:1094–1100. https://doi.org/10.1002/mawe.200300717

[18] Ding HH, Fridrici V, Geringer J, Fontaine J, Kapsa Ph. Influence of diamond-like carbon coatings and roughness on fretting behaviors of Ti–6Al–4V for neck adapter–femoral stem contact. Wear 2018;406–407:53–67. https://doi.org/10.1016/j.wear.2018.04.001

[19] Robertson J. Diamond-like amorphous carbon. Mater Sci Eng R 2002;37:129–281. https://doi.org/10.1016/S0927-796X(02)00005-0

[20] Koshigan KD, Mangolini F, McClimon JB, Vacher B, Bec S, Carpick RW, Fontaine J. Understanding the hydrogen and oxygen gas pressure dependence of the tribological properties of silicon oxide–doped hydrogenated amorphous carbon coatings. Carbon 2015;93:851–860. https://doi.org/10.1016/j.carbon.2015.06.004

[21] Kunze T, Posselt M, Gemming S, Seifert G, Konicek AR, Carpick RW, Pastewka L, Moseler M. Wear, plasticity, and rehybridization in tetrahedral amorphous carbon. Tribol Lett 2014;53:119–126. https://doi.org/10.1007/s11249-013-0250-7

[22] Liu Y, Erdemir A, Meletis EI. A study of the wear mechanism of diamond-like carbon films. Surf Coat Technol 1996;82:48–56. https://doi.org/10.1016/0257-8972(95)02623-1

[23] Hirvonen J-P, Lappalainen R, Koskinen J, Anttila A, Jervis TR, Trkula M. Tribological characteristics of diamond-like films deposited with an arc-discharge method. J Mater Res 1990;5:2524–2530. https://doi.org/10.1557/JMR.1990.2524

[24] Ronkainen H, Koskinen J, Likonen J, Varjus S, Vihersalo J. Characterization of wear

surfaces in dry sliding of steel and alumina on hydrogenated and hydrogen-free carbon films. Diam Relat Mater 1994;3:1329–1336. https://doi.org/10.1016/0925-9635(94)90147-3

[25] Donnet C, Fontaine J, Grill A, Mogne TL. The role of hydrogen on the friction mechanism of diamond-like carbon films. Tribol Lett 2001;9:137–142. https://doi.org/10.1023/A:1018800719806

[26] Konicek AR, Grierson DS, Gilbert PUPA, Sawyer WG, Sumant AV, Carpick RW. Origin of ultralow friction and wear in ultrananocrystalline diamond. Phys Rev Lett 2008;100:235502. https://doi.org/10.1103/PhysRevLett.100.235502

[27] Machine TSD 550, from HEF. http://www.tshungary.hu/dok/DLC_coating_equipment.pdf

[28] Fridrici V, Fouvry S, Kapsa Ph. Fretting wear behavior of a Cu–Ni–In plasma coating. Surf Coat Technol 2003;163–164:429–434. https://doi.org/10.1016/S0257-8972(02)00639-4

[29] Ding HH, Fridrici V, Geringer J, Fontaine J, Kapsa Ph. Influence of diamond-like carbon coatings and roughness on fretting behaviors of Ti–6Al–4V for neck adapter–femoral stem contact. Wear 2018;406-407:53–67. https://doi.org/10.1016/j.wear.2018.04.001

[30] Ding HH, Fridrici V, Bouvard G, Geringer J, Kapsa Ph. Influence of calf serum on fretting behaviors of Ti–6Al–4V and diamond-like carbon coating for neck adapter–femoral stem contact. Tribol Lett 2018;66:110. https://doi.org/10.1007/s11249-018-1069-z

[31] Fouvry S, Kapsa Ph, Vincent L. Analysis of sliding behaviour for fretting loadings: determination of transition criteria. Wear 1995;185:35–46. https://doi.org/10.1016/0043-1648(94)06582-9

[32] Koshigan KD. Understanding the influence of environment on the solid lubrication processes of carbon-based thin films (PhD thesis). Ecully, Ecole centrale de Lyon, 2015. http://bibli.ec-lyon.fr/exl-doc/TH_T2491_kkoshigan.pdf

[33] Ferrari AC. Determination of bonding in diamond-like carbon by Raman spectroscopy. Diam Relat Mater 2002;11:1053–1061. https://doi.org/10.1016/S0925-9635(01)00730-0

[34] Tai FC, Lee SC, Chen J, Wei C, Chang SH. Multipeak fitting analysis of Raman spectra on DLCH film. J Raman Spectrosc 2009;40:1055–1059. https://doi.org/10.1002/jrs.2234

Captions of figures

Fig. 1. Neck adapter/femoral stem contact: XO Femoral Stems with modular neck adapter, from the company SEM Science et Médecine, established in France [3]. Both the neck adapter and femoral stem are made of Ti–6Al–4V alloy.

Fig. 2. (a) Coating response wear map and (b) evolution of friction coefficient for representative tests under low and high load conditions [18]. Tests were conducted with a DLC coated rough flat/rough Ti–6Al–4V cylinder contact.

Fig. 3. SEM and EDX of cross sections of flat samples: (a) rough flat; (b) smooth flat.

Fig. 4. 3D topography of (a) the neck-adapter surface and (b) the femoral-stem inner surface.

Fig. 5. 3D topography of flat and cylinder samples: (a) smooth flat without coating; (b) rough flat without coating; (c) rough cylinder without coating; (d) smooth flat with DLC coating; (e) rough flat with DLC coating.

Fig. 6. Surface roughness of flat and cylinder samples.

Fig. 7. (a) Nano-hardness and (b) elastic modulus of DLC coating on smooth flat and of Ti–6Al–4V substrate.

Fig. 8. (a) Schematic outline of the fretting-wear machine and (b) geometry of flat and cylinder samples.

Fig. 9. (a) Evolution of friction coefficient with number of cycles (logarithmic scale) for rough and smooth flats without and with DLC coating. Fretting logs for tests (b) on rough flat without DLC coating; (c) on smooth flat without DLC coating; (d) on rough flat with DLC coating; (e) on smooth flat with DLC coating.

Fig. 10. Schematic diagram for three series of tests.

Fig. 11. Friction coefficient evolution vs cycle number for tests with DLC coating: (a) rough flat; (b) smooth flat.

Fig. 12. Ti–6Al–4V surface (in contact with DLC coated rough flat) at cycle number 0.

Fig. 13. Rough DLC coating surface (in contact with Ti–6Al–4V surface) at cycle number 0.

Fig. 14. Ti–6Al–4V surface (in contact with DLC coated smooth flat) at cycle number 0.

Fig. 15. Smooth DLC coating surface (in contact with Ti–6Al–4V surface) at cycle number 0.

Fig. 16. (a), (c) Ti–6Al–4V surface in contact with (b), (d) rough DLC coating surface after 1 cycle.

Fig. 17. (a) Ti–6Al–4V surface in contact with (b) smooth DLC coating surface after 1 cycle.

Fig. 18. Ti–6Al–4V surface (in contact with DLC coated rough flat) after 20 cycles.

Fig. 19. Rough DLC coating surface (in contact with Ti–6Al–4V surface) after 20 cycles.

Fig. 20. Ti–6Al–4V surface (in contact with DLC coated rough flat) after 40 cycles.

Fig. 1

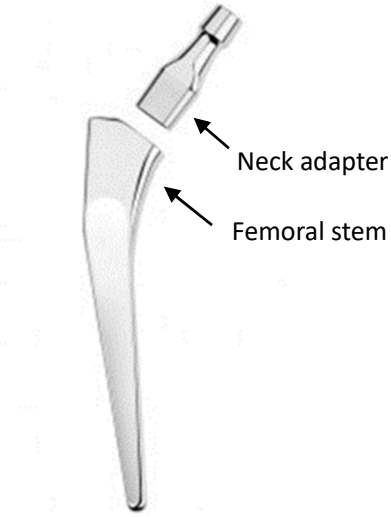

Fig. 2

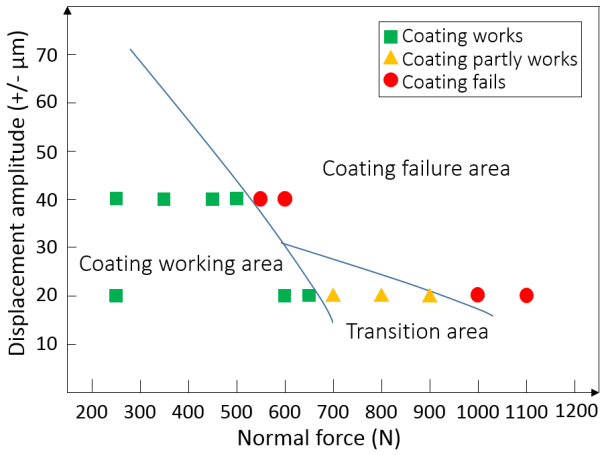
Coating works
Coating partly works
Coating fails
Coating failure area
Coating working area
Transition area
Displacement amplitude (+/- µm)
Normal force (N)
10
20
30
40
50
60
70
200
300
400
500
600
700
800
900
1000
1100
1200

(a)

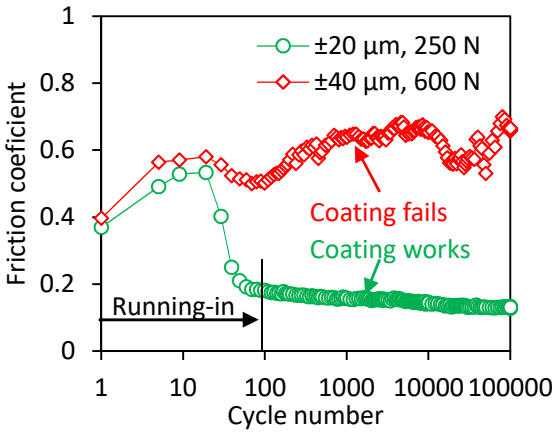
±20 µm, 250 N
±40 µm, 600 N
Coating fails
Coating works
Running-in
Friction coeficient
Cycle number
0
0.2
0.4
0.6
0.8
1
1
10
100
1000
10000
100000

(b)

Fig. 3

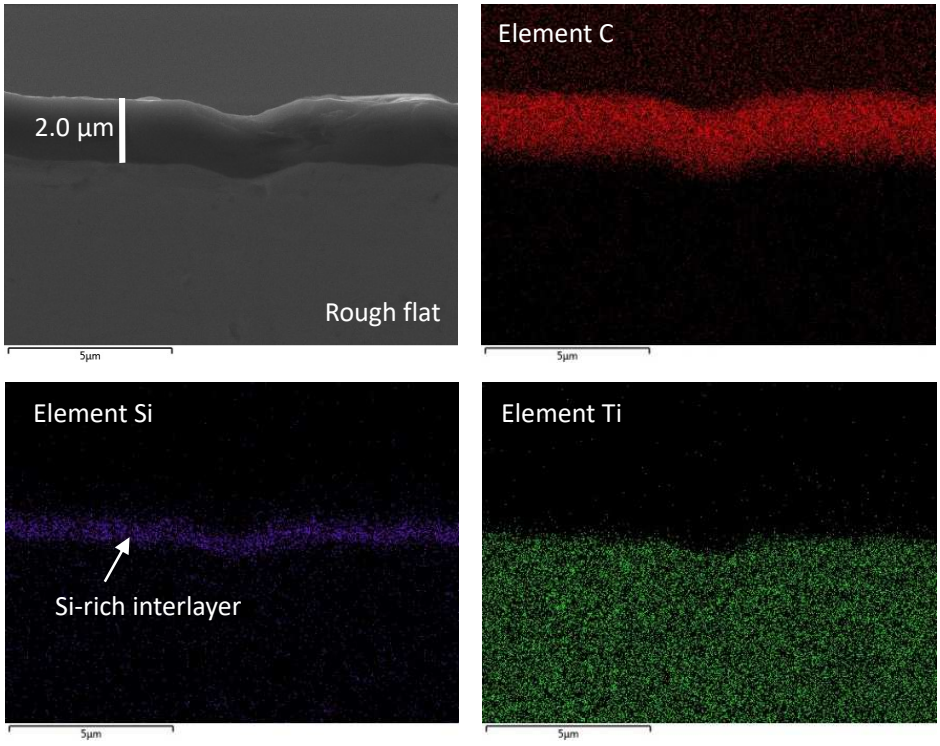
2.0 µm
Rough flat
Element C
Element Si
Si-rich interlayer
Element Ti

(a)

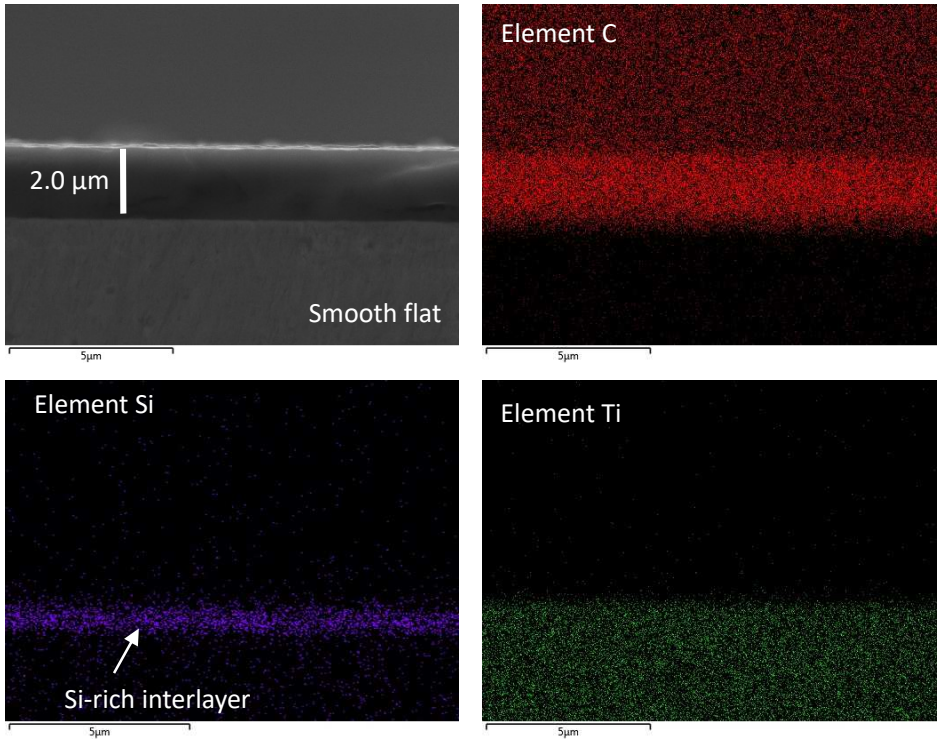
2.0 µm
Smooth flat
Element C
Element Si
Si-rich interlayer
Element Ti

(b)

Fig. 4

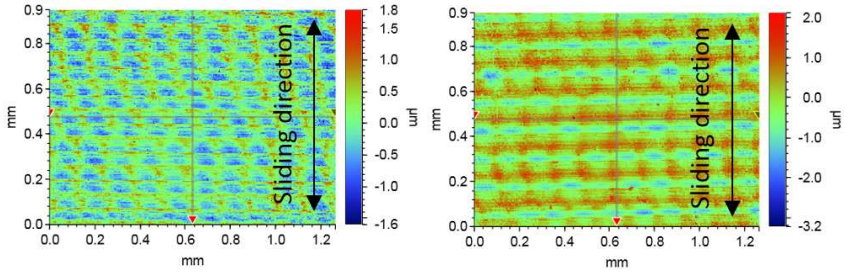

(a) (b)

Fig. 5

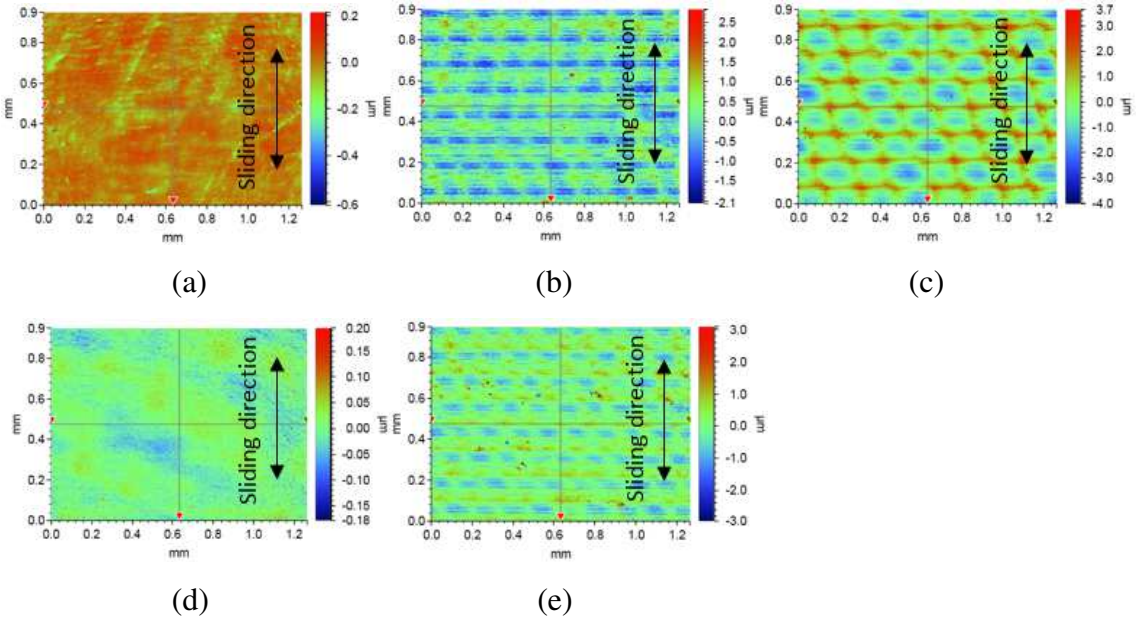

Fig. 6

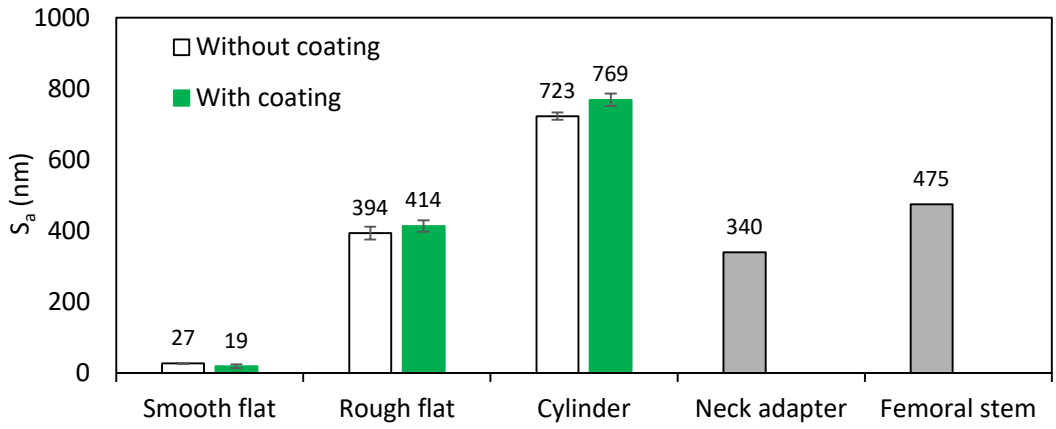
1000
800
600
400
200
0
S_a (nm)
Without coating
With coating
27
19
394
414
723
769
340
475
Smooth flat
Rough flat
Cylinder
Neck adapter
Femoral stem

Fig. 7

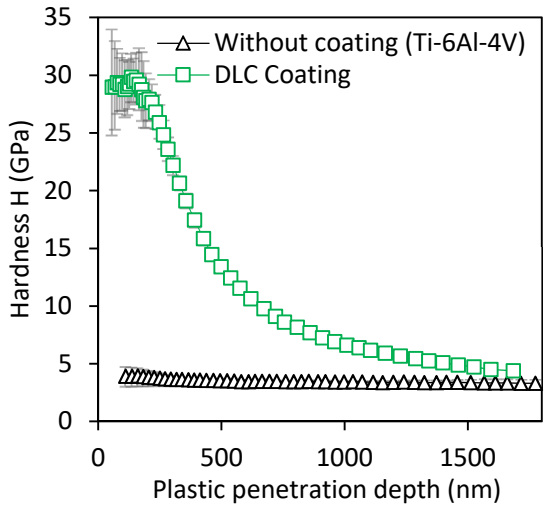
Without coating (Ti-6Al-4V)
DLC Coating
Hardness H (GPa)
Plastic penetration depth (nm)
0
5
10
15
20
25
30
35
0
500
1000
1500

(a)

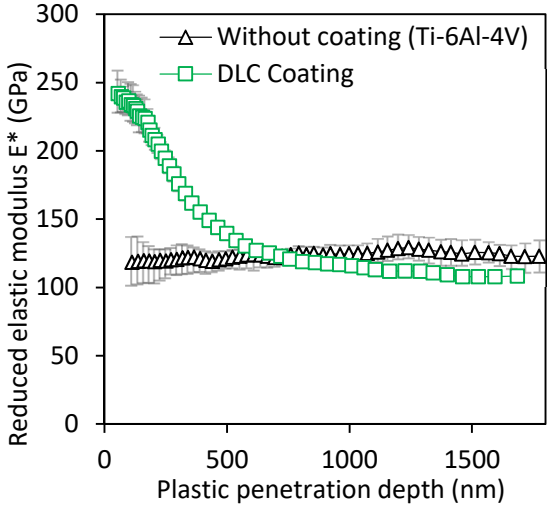
Without coating (Ti-6Al-4V)
DLC Coating
Reduced elastic modulus E* (GPa)
Plastic penetration depth (nm)
0
50
100
150
200
250
300
0
500
1000
1500

(b)

Fig. 8

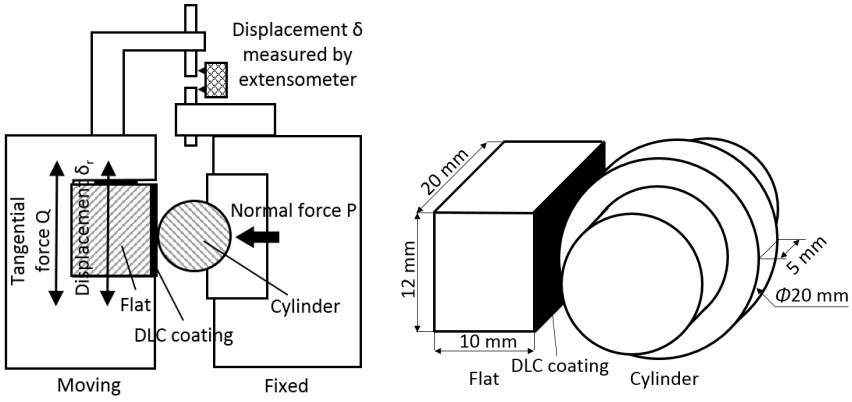
Displacement δ
measured by
extensometer
Tangential
force Q
Displacement δt
Normal force P
Flat
Cylinder
DLC coating
Moving
Fixed
20 mm
12 mm
5 mm
Φ20 mm
10 mm
Flat
DLC coating
Cylinder

(a) (b)

Fig. 9

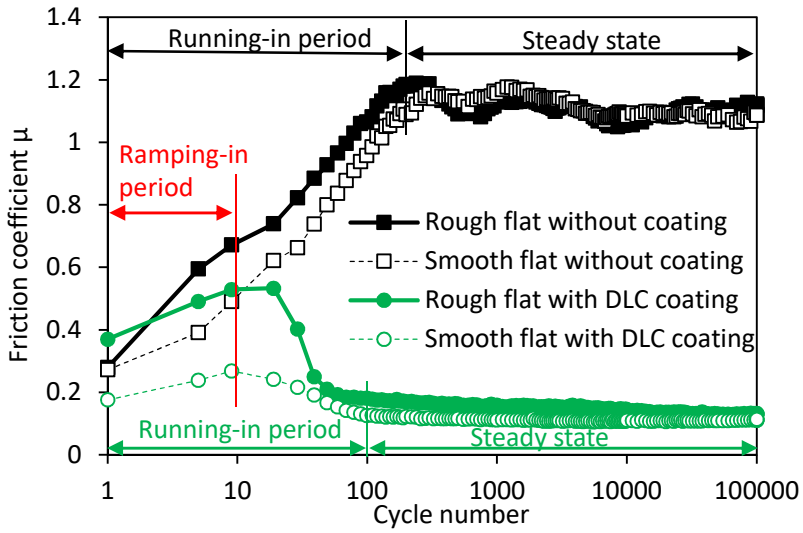
Running-in period
Steady state
Ramping-in period
Friction coefficient μ
Rough flat without coating
Smooth flat without coating
Rough flat with DLC coating
Smooth flat with DLC coating
Running-in period
Steady state
Cycle number

(a)

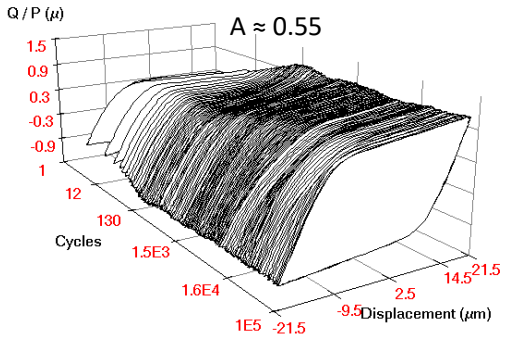
Q / P (μ)
A ≈ 0.55
Cycles
Displacement (μm)

(b)

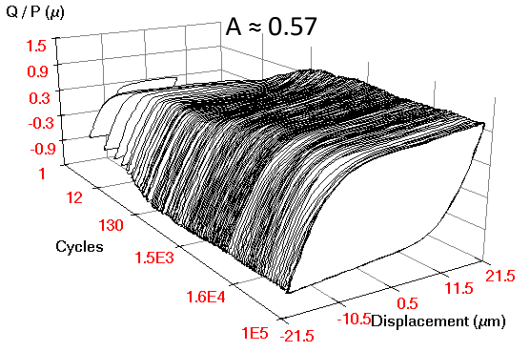
Q / P (μ)
A ≈ 0.57
Cycles
Displacement (μm)

(c)

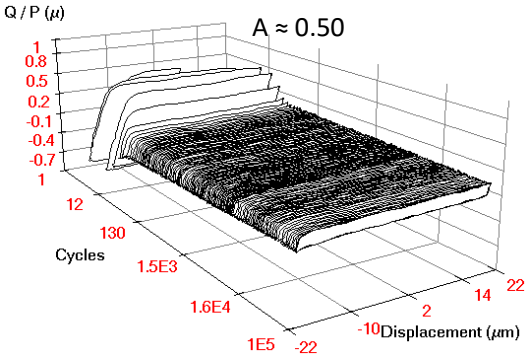
Q / P (μ)
A ≈ 0.50
Cycles
Displacement (μm)

(d)

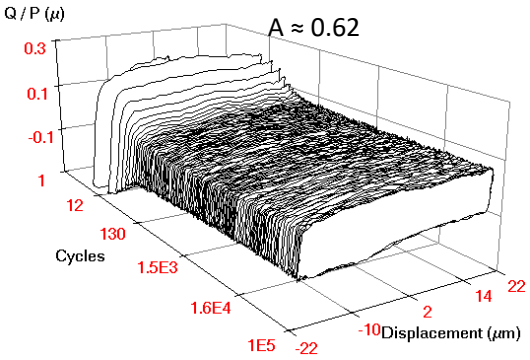
Q / P (μ)
A ≈ 0.62
Cycles
Displacement (μm)

(e)

Fig. 10

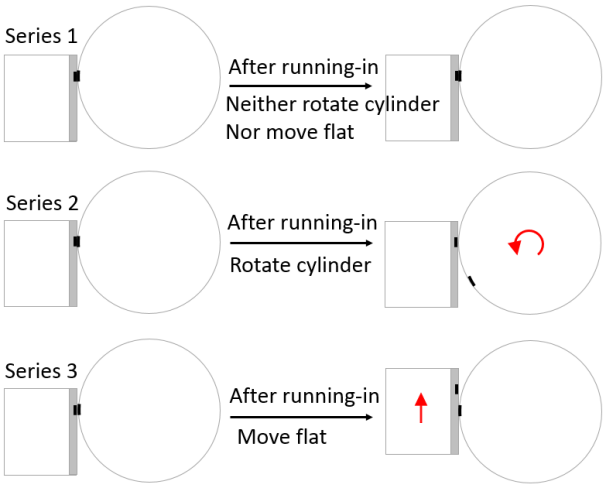
Series 1
After running-in
Neither rotate cylinder
Nor move flat
Series 2
After running-in
Rotate cylinder
Series 3
After running-in
Move flat

Fig. 11

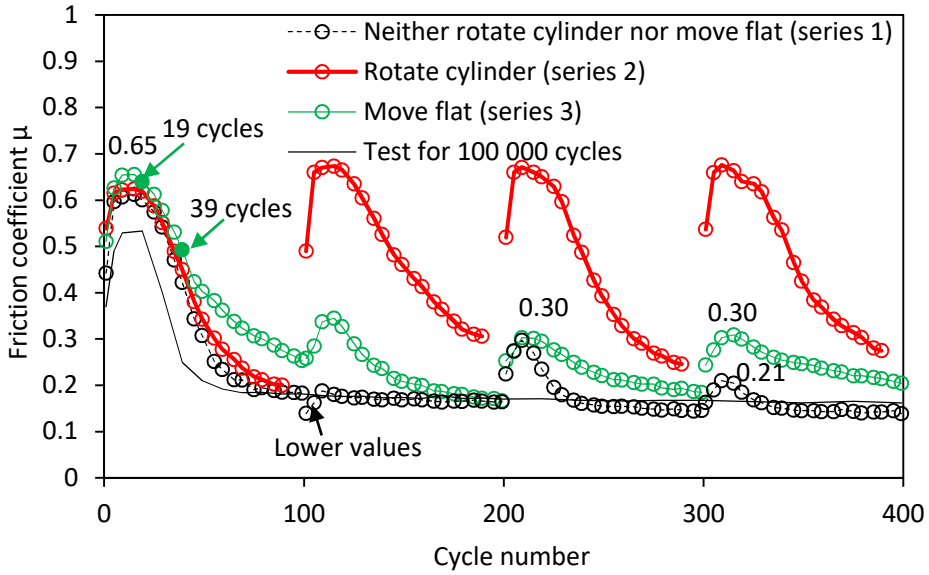
Neither rotate cylinder nor move flat (series 1)
Rotate cylinder (series 2)
Move flat (series 3)
Test for 100 000 cycles
Friction coefficient μ
Cycle number
0.65
19 cycles
39 cycles
0.30
0.30
0.21
Lower values
0
0.1
0.2
0.3
0.4
0.5
0.6
0.7
0.8
0.9
1
0
100
200
300
400

(a)

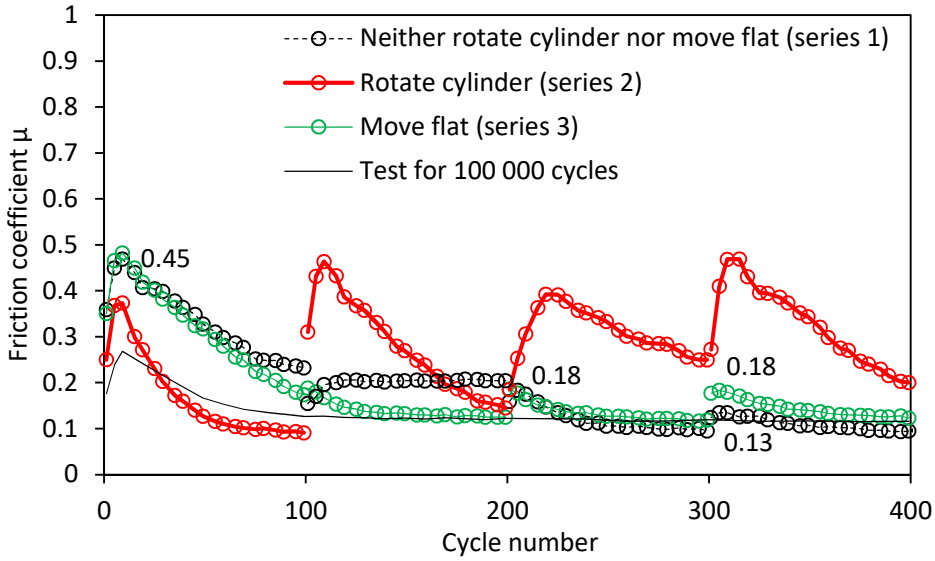
Neither rotate cylinder nor move flat (series 1)
Rotate cylinder (series 2)
Move flat (series 3)
Test for 100 000 cycles
Friction coefficient μ
Cycle number
0.45
0.18
0.18
0.13
0
0.1
0.2
0.3
0.4
0.5
0.6
0.7
0.8
0.9
1
0
100
200
300
400

(b)

Fig. 12

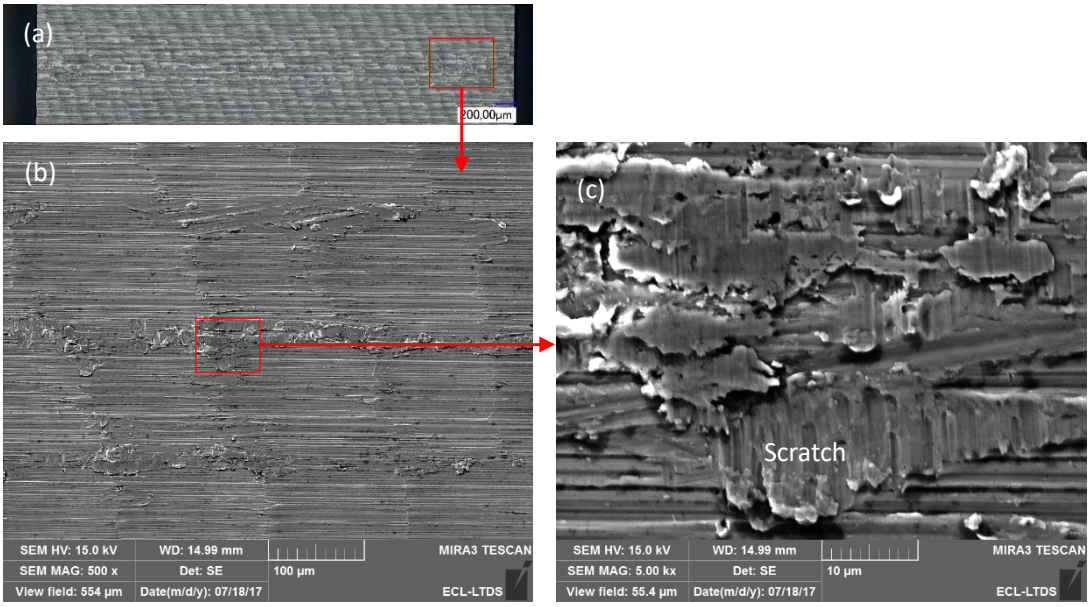
(a)
200.00µm
(b)
SEM HV: 15.0 kV
WD: 14.99 mm
MIRA3 TESCAN
SEM MAG: 500 x
Det: SE
100 µm
View field: 554 µm
Date(m/d/y): 07/18/17
ECL-LTDS
(c)
Scratch
SEM HV: 15.0 kV
WD: 14.99 mm
MIRA3 TESCAN
SEM MAG: 5.00 kx
Det: SE
10 µm
View field: 55.4 µm
Date(m/d/y): 07/18/17
ECL-LTDS

Fig. 13

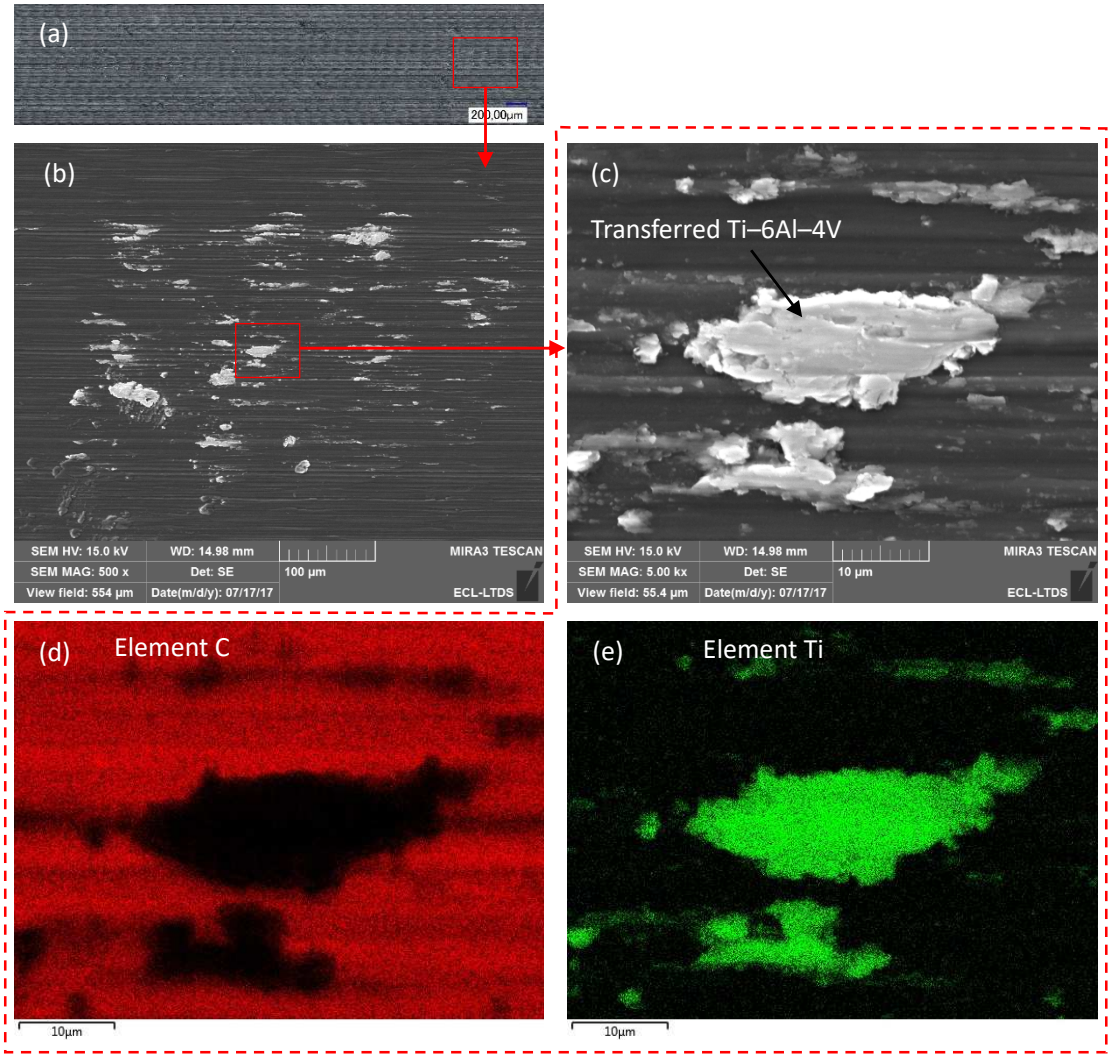
(a)
200.00μm
(b)
SEM HV: 15.0 kV
WD: 14.98 mm
MIRA3 TESCAN
SEM MAG: 500 x
Det: SE
100 μm
View field: 554 μm
Date(m/d/y): 07/17/17
ECL-LTDS
(c)
Transferred Ti–6Al–4V
SEM HV: 15.0 kV
WD: 14.98 mm
MIRA3 TESCAN
SEM MAG: 5.00 kx
Det: SE
10 μm
View field: 55.4 μm
Date(m/d/y): 07/17/17
ECL-LTDS
(d)
Element C
10μm
(e)
Element Ti
10μm

Fig. 14

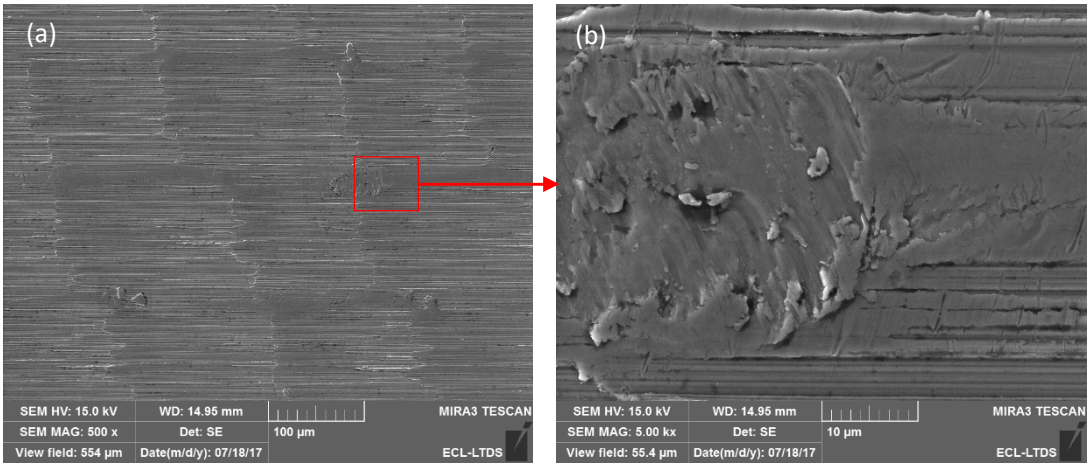
(a)
SEM HV: 15.0 kV
WD: 14.95 mm
MIRA3 TESCAN
SEM MAG: 500 x
Det: SE
100 µm
View field: 554 µm
Date(m/d/y): 07/18/17
ECL-LTDS
(b)
SEM HV: 15.0 kV
WD: 14.95 mm
MIRA3 TESCAN
SEM MAG: 5.00 kx
Det: SE
10 µm
View field: 55.4 µm
Date(m/d/y): 07/18/17
ECL-LTDS

Fig. 15

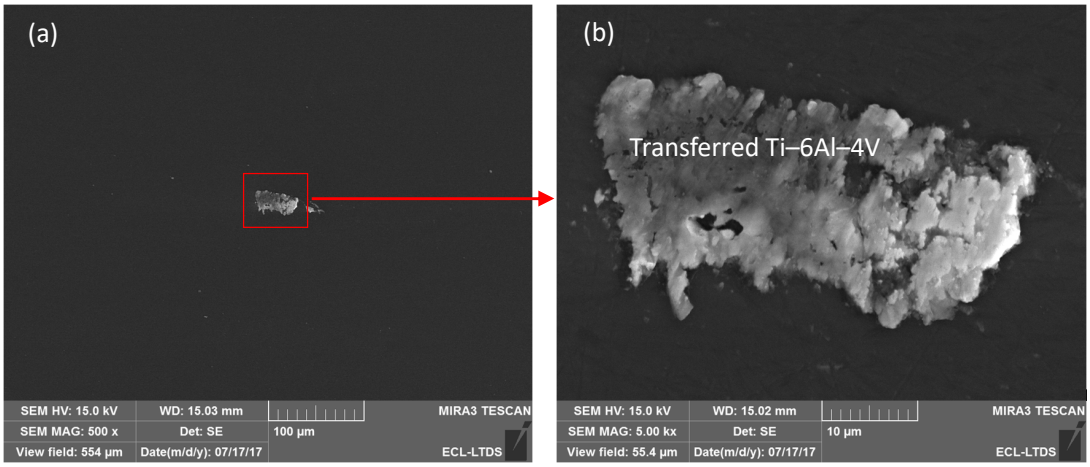
(a)
(b)
Transferred Ti–6Al–4V
SEM HV: 15.0 kV
WD: 15.03 mm
MIRA3 TESCAN
SEM MAG: 500 x
Det: SE
100 µm
View field: 554 µm
Date(m/d/y): 07/17/17
ECL-LTDS
SEM HV: 15.0 kV
WD: 15.02 mm
MIRA3 TESCAN
SEM MAG: 5.00 kx
Det: SE
10 µm
View field: 55.4 µm
Date(m/d/y): 07/17/17
ECL-LTDS

Fig. 16

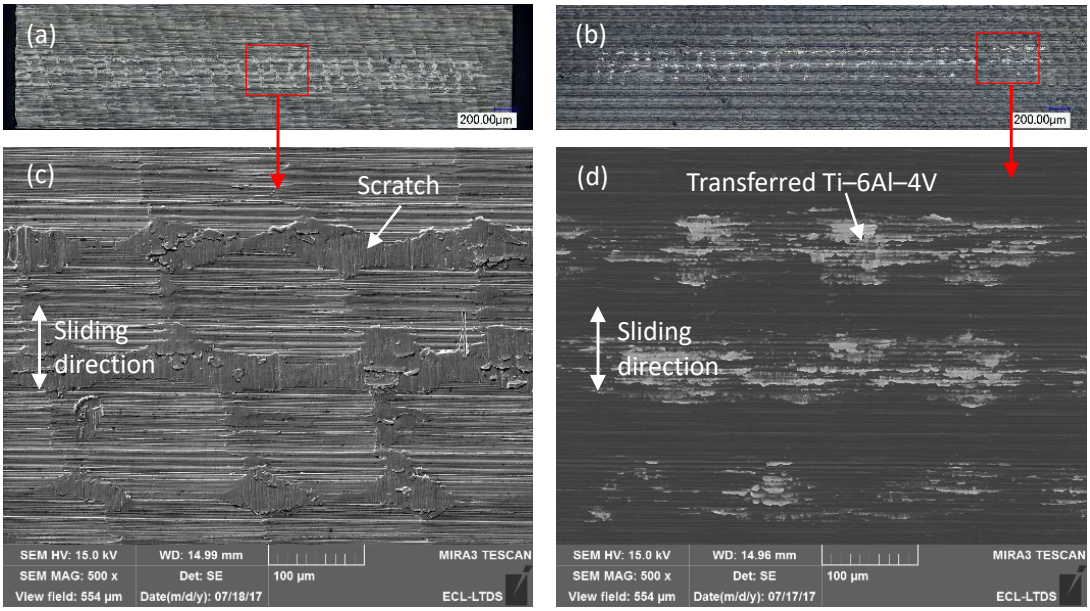
(a)
200.00μm
(b)
200.00μm
(c)
Scratch
Sliding direction
SEM HV: 15.0 kV
WD: 14.99 mm
MIRA3 TESCAN
SEM MAG: 500 x
Det: SE
100 μm
View field: 554 μm
Date(m/d/y): 07/18/17
ECL-LTDS
(d)
Transferred Ti–6Al–4V
Sliding direction
SEM HV: 15.0 kV
WD: 14.96 mm
MIRA3 TESCAN
SEM MAG: 500 x
Det: SE
100 μm
View field: 554 μm
Date(m/d/y): 07/17/17
ECL-LTDS

Fig. 17

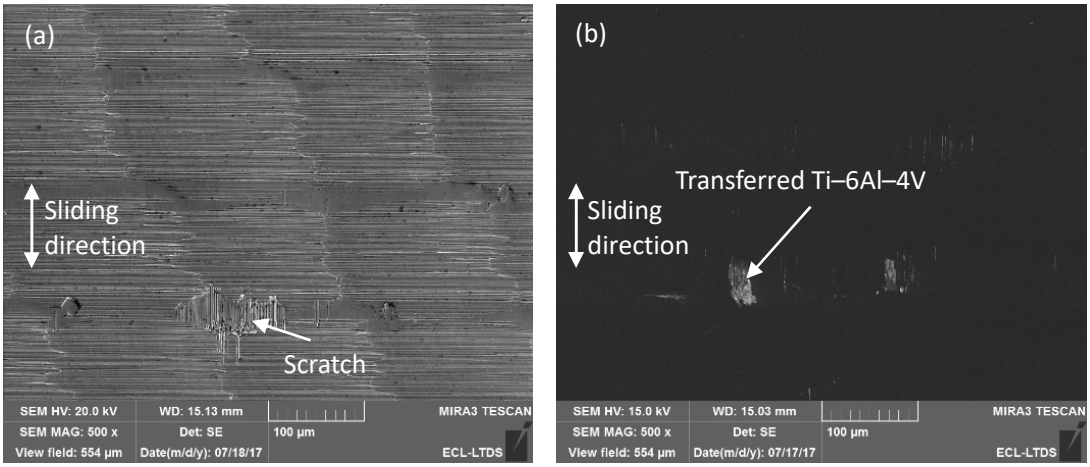
(a)
Sliding direction
Scratch
SEM HV: 20.0 kV
WD: 15.13 mm
MIRA3 TESCAN
SEM MAG: 500 x
Det: SE
100 µm
View field: 554 µm
Date(m/d/y): 07/18/17
ECL-LTDS
(b)
Transferred Ti–6Al–4V
Sliding direction
SEM HV: 15.0 kV
WD: 15.03 mm
MIRA3 TESCAN
SEM MAG: 500 x
Det: SE
100 µm
View field: 554 µm
Date(m/d/y): 07/17/17
ECL-LTDS

Fig. 18

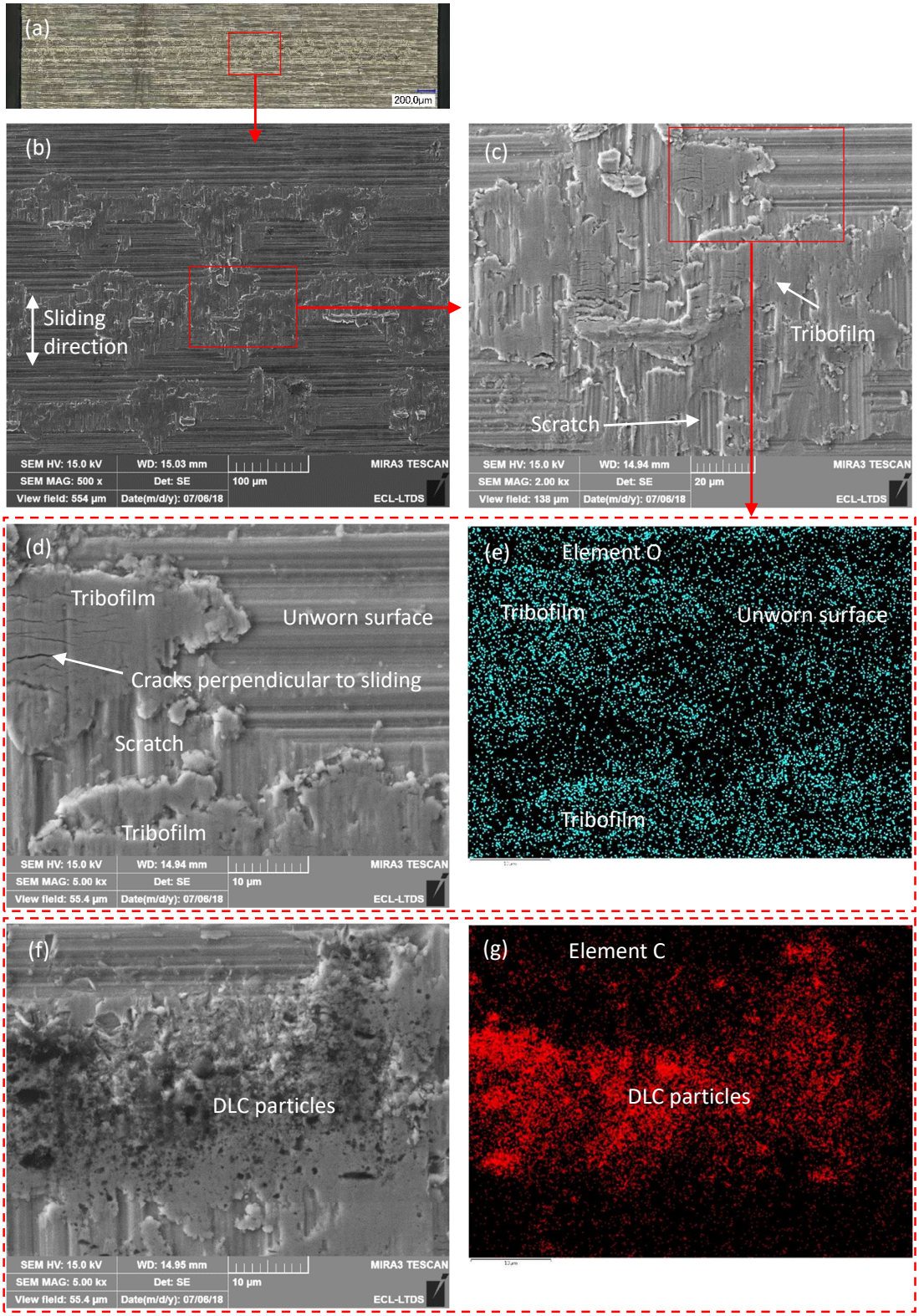
(a)
200,0µm
(b)
Sliding direction
SEM HV: 15.0 kV
WD: 15.03 mm
MIRA3 TESCAN
SEM MAG: 500 x
Det: SE
100 µm
View field: 554 µm
Date(m/d/y): 07/06/18
ECL-LTDS
(c)
Tribofilm
Scratch
SEM HV: 15.0 kV
WD: 14.94 mm
MIRA3 TESCAN
SEM MAG: 2.00 kx
Det: SE
20 µm
View field: 138 µm
Date(m/d/y): 07/06/18
ECL-LTDS
(d)
Tribofilm
Unworn surface
Cracks perpendicular to sliding
Scratch
Tribofilm
SEM HV: 15.0 kV
WD: 14.94 mm
MIRA3 TESCAN
SEM MAG: 5.00 kx
Det: SE
10 µm
View field: 55.4 µm
Date(m/d/y): 07/06/18
ECL-LTDS
(e)
Element O
Tribofilm
Unworn surface
Tribofilm
(f)
DLC particles
SEM HV: 15.0 kV
WD: 14.95 mm
MIRA3 TESCAN
SEM MAG: 5.00 kx
Det: SE
10 µm
View field: 55.4 µm
Date(m/d/y): 07/06/18
ECL-LTDS
(g)
Element C
DLC particles

Fig. 19

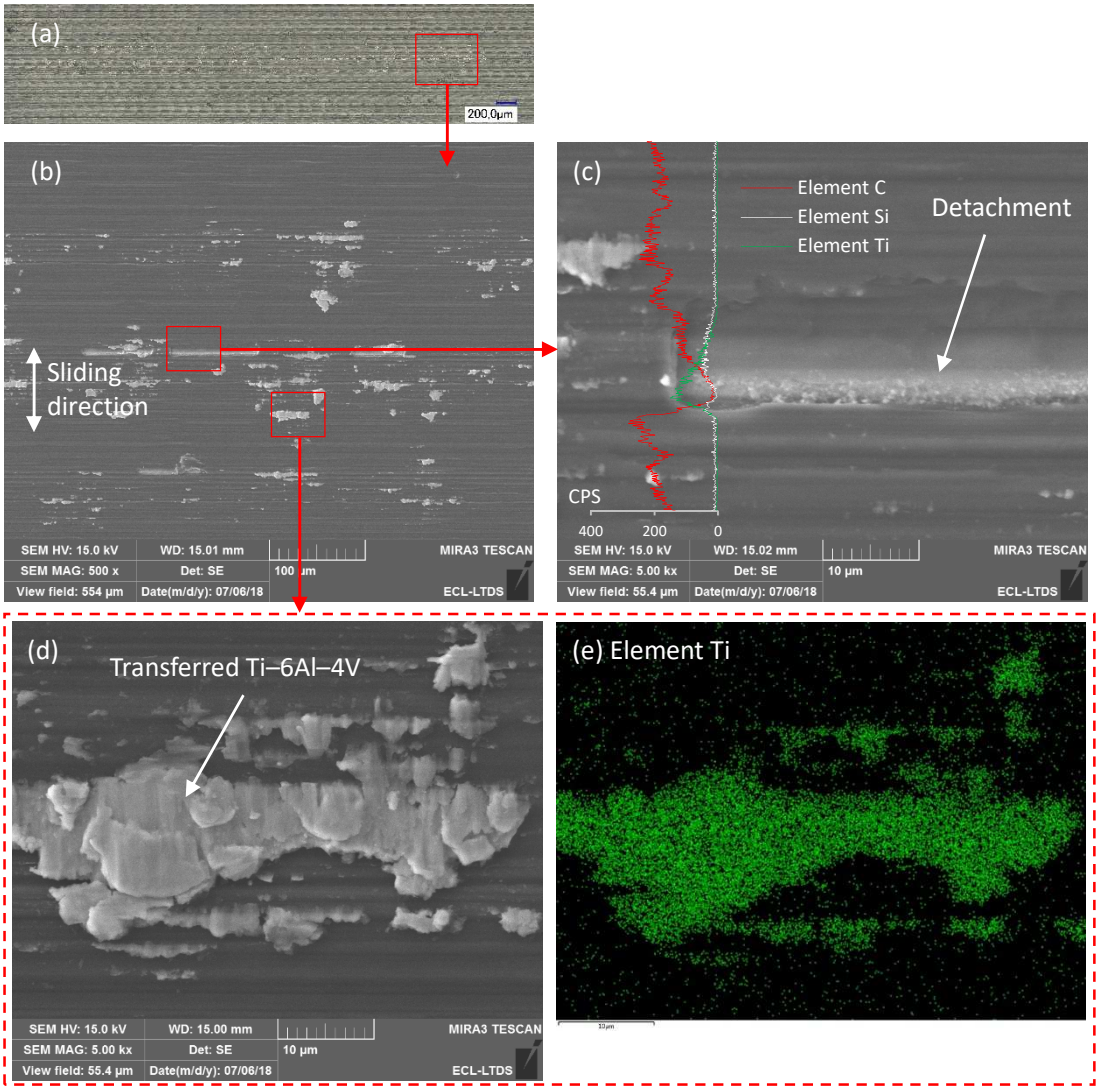
(a)
200.0μm
(b)
Sliding direction
SEM HV: 15.0 kV
WD: 15.01 mm
MIRA3 TESCAN
SEM MAG: 500 x
Det: SE
100 μm
View field: 554 μm
Date(m/d/y): 07/06/18
ECL-LTDS
(c)
Element C
Element Si
Element Ti
Detachment
CPS
400
200
0
SEM HV: 15.0 kV
WD: 15.02 mm
MIRA3 TESCAN
SEM MAG: 5.00 kx
Det: SE
10 μm
View field: 55.4 μm
Date(m/d/y): 07/06/18
ECL-LTDS
(d)
Transferred Ti–6Al–4V
SEM HV: 15.0 kV
WD: 15.00 mm
MIRA3 TESCAN
SEM MAG: 5.00 kx
Det: SE
10 μm
View field: 55.4 μm
Date(m/d/y): 07/06/18
ECL-LTDS
(e) Element Ti

Fig. 20

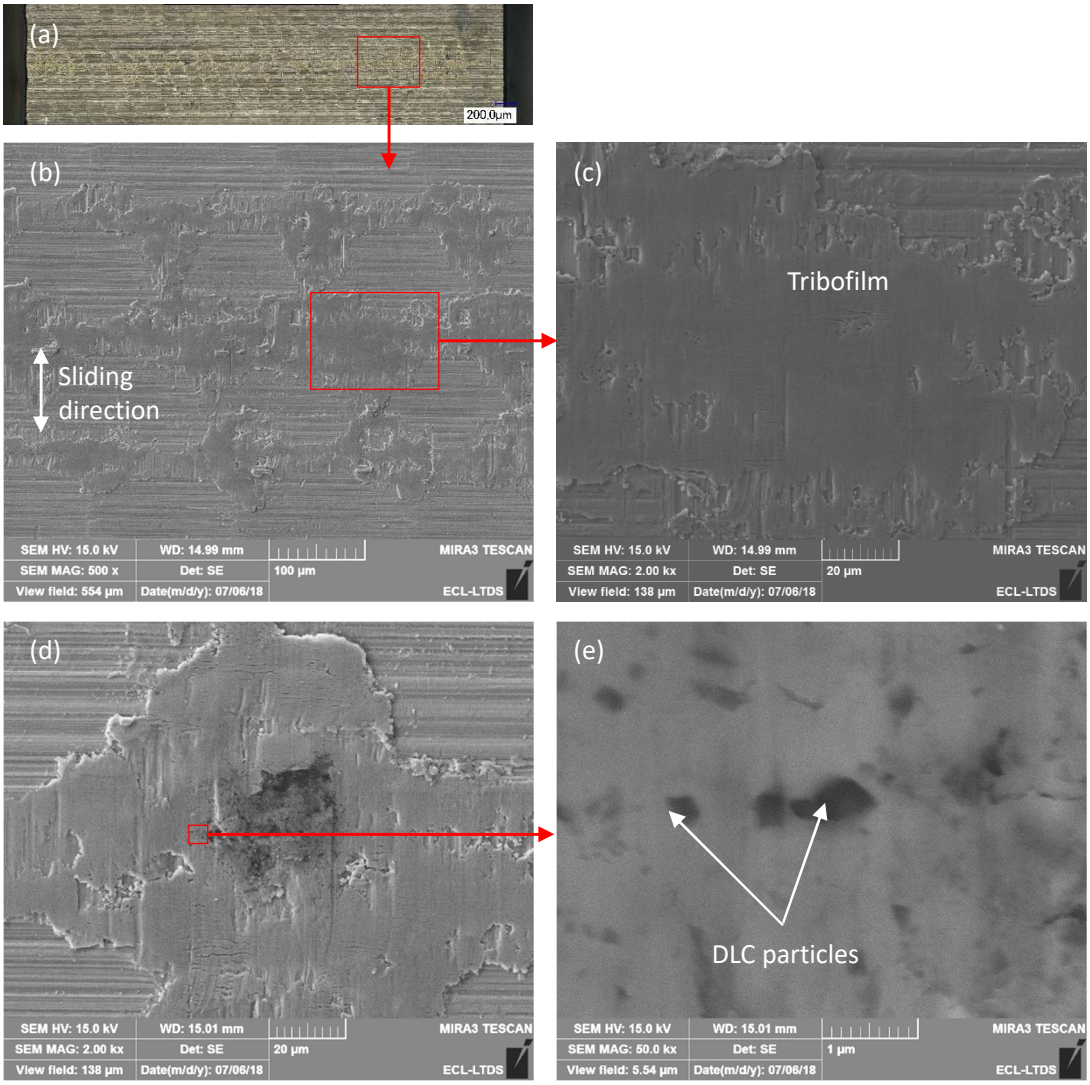
(a)
200.0µm
(b)
Sliding
direction
SEM HV: 15.0 kV
WD: 14.99 mm
MIRA3 TESCAN
SEM MAG: 500 x
Det: SE
100 µm
View field: 554 µm
Date(m/d/y): 07/06/18
ECL-LTDS
(c)
Tribofilm
SEM HV: 15.0 kV
WD: 14.99 mm
MIRA3 TESCAN
SEM MAG: 2.00 kx
Det: SE
20 µm
View field: 138 µm
Date(m/d/y): 07/06/18
ECL-LTDS
(d)
SEM HV: 15.0 kV
WD: 15.01 mm
MIRA3 TESCAN
SEM MAG: 2.00 kx
Det: SE
20 µm
View field: 138 µm
Date(m/d/y): 07/06/18
ECL-LTDS
(e)
DLC particles
SEM HV: 15.0 kV
WD: 15.01 mm
MIRA3 TESCAN
SEM MAG: 50.0 kx
Det: SE
1 µm
View field: 5.54 µm
Date(m/d/y): 07/06/18
ECL-LTDS

Fig. 21

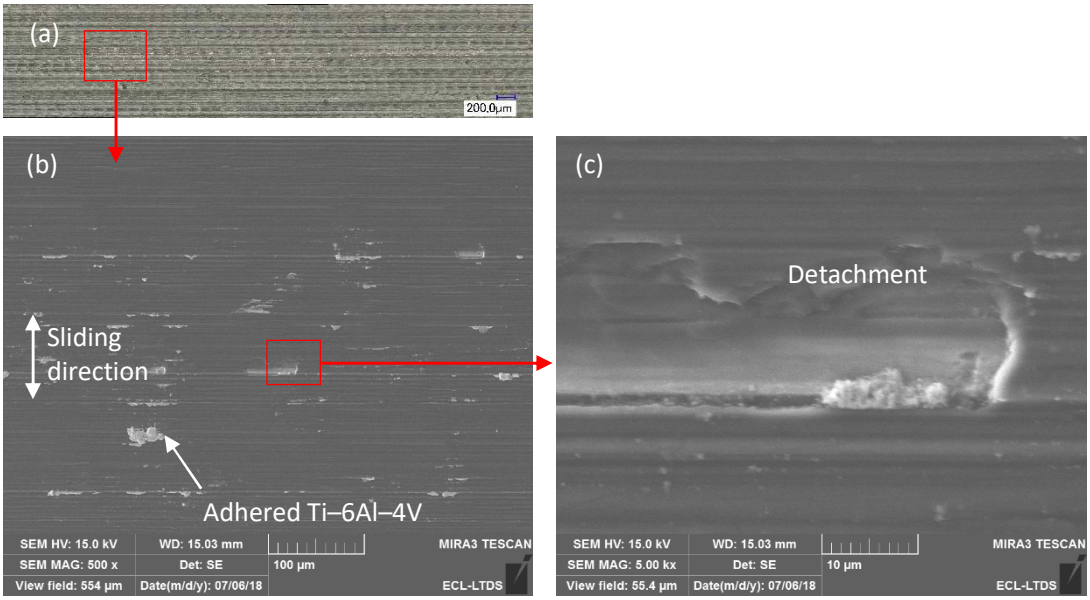
(a)
200.0µm
(b)
Sliding
direction
Adhered Ti–6Al–4V
SEM HV: 15.0 kV
WD: 15.03 mm
MIRA3 TESCAN
SEM MAG: 500 x
Det: SE
100 µm
View field: 554 µm
Date(m/d/y): 07/06/18
ECL-LTDS
(c)
Detachment
SEM HV: 15.0 kV
WD: 15.03 mm
MIRA3 TESCAN
SEM MAG: 5.00 kx
Det: SE
10 µm
View field: 55.4 µm
Date(m/d/y): 07/06/18
ECL-LTDS

Fig. 22

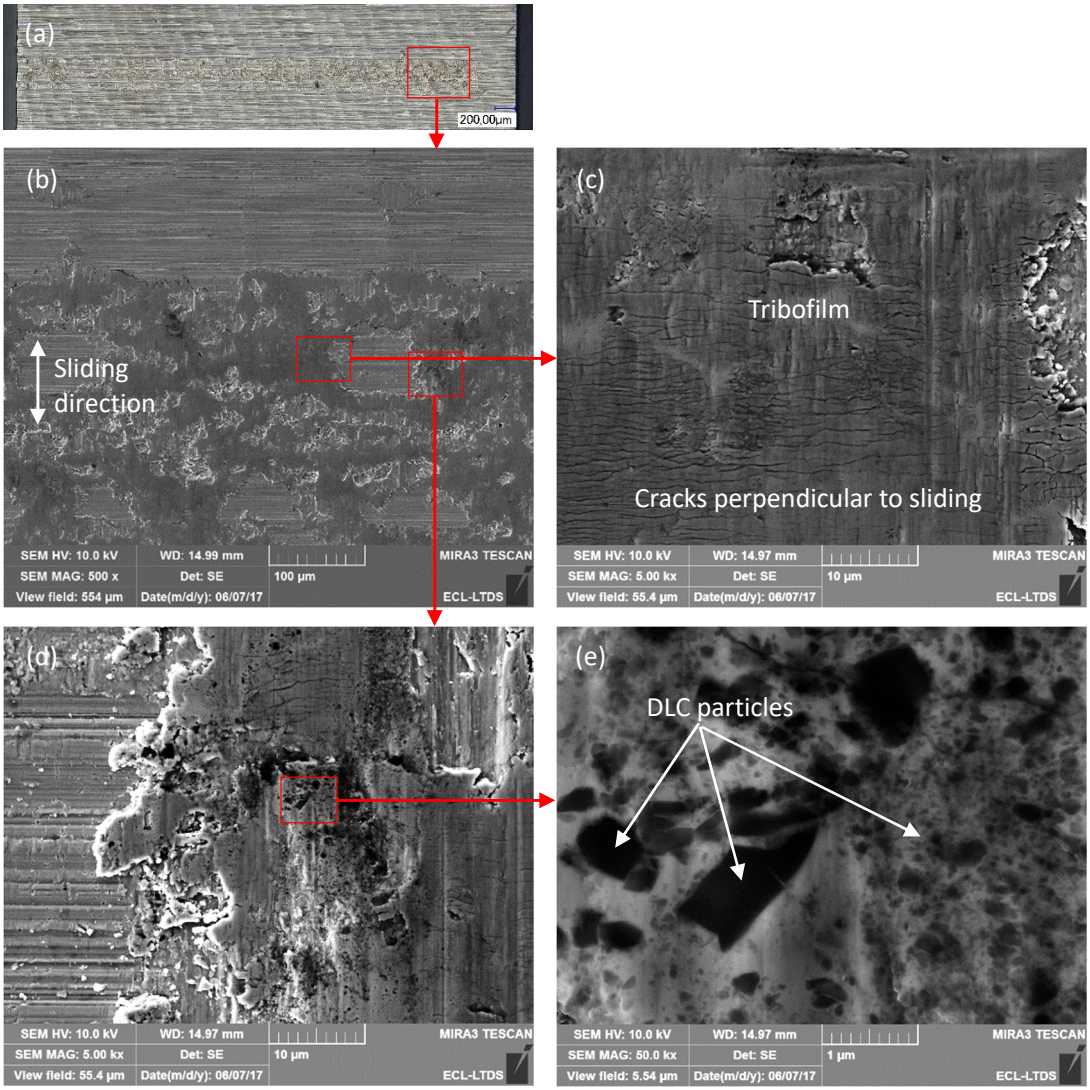
(a)
200.00µm
(b)
Sliding direction
SEM HV: 10.0 kV
WD: 14.99 mm
MIRA3 TESCAN
SEM MAG: 500 x
Det: SE
100 µm
View field: 554 µm
Date(m/d/y): 06/07/17
ECL-LTDS
(c)
Tribofilm
Cracks perpendicular to sliding
SEM HV: 10.0 kV
WD: 14.97 mm
MIRA3 TESCAN
SEM MAG: 5.00 kx
Det: SE
10 µm
View field: 55.4 µm
Date(m/d/y): 06/07/17
ECL-LTDS
(d)
SEM HV: 10.0 kV
WD: 14.97 mm
MIRA3 TESCAN
SEM MAG: 5.00 kx
Det: SE
10 µm
View field: 55.4 µm
Date(m/d/y): 06/07/17
ECL-LTDS
(e)
DLC particles
SEM HV: 10.0 kV
WD: 14.97 mm
MIRA3 TESCAN
SEM MAG: 50.0 kx
Det: SE
1 µm
View field: 5.54 µm
Date(m/d/y): 06/07/17
ECL-LTDS

Fig. 23

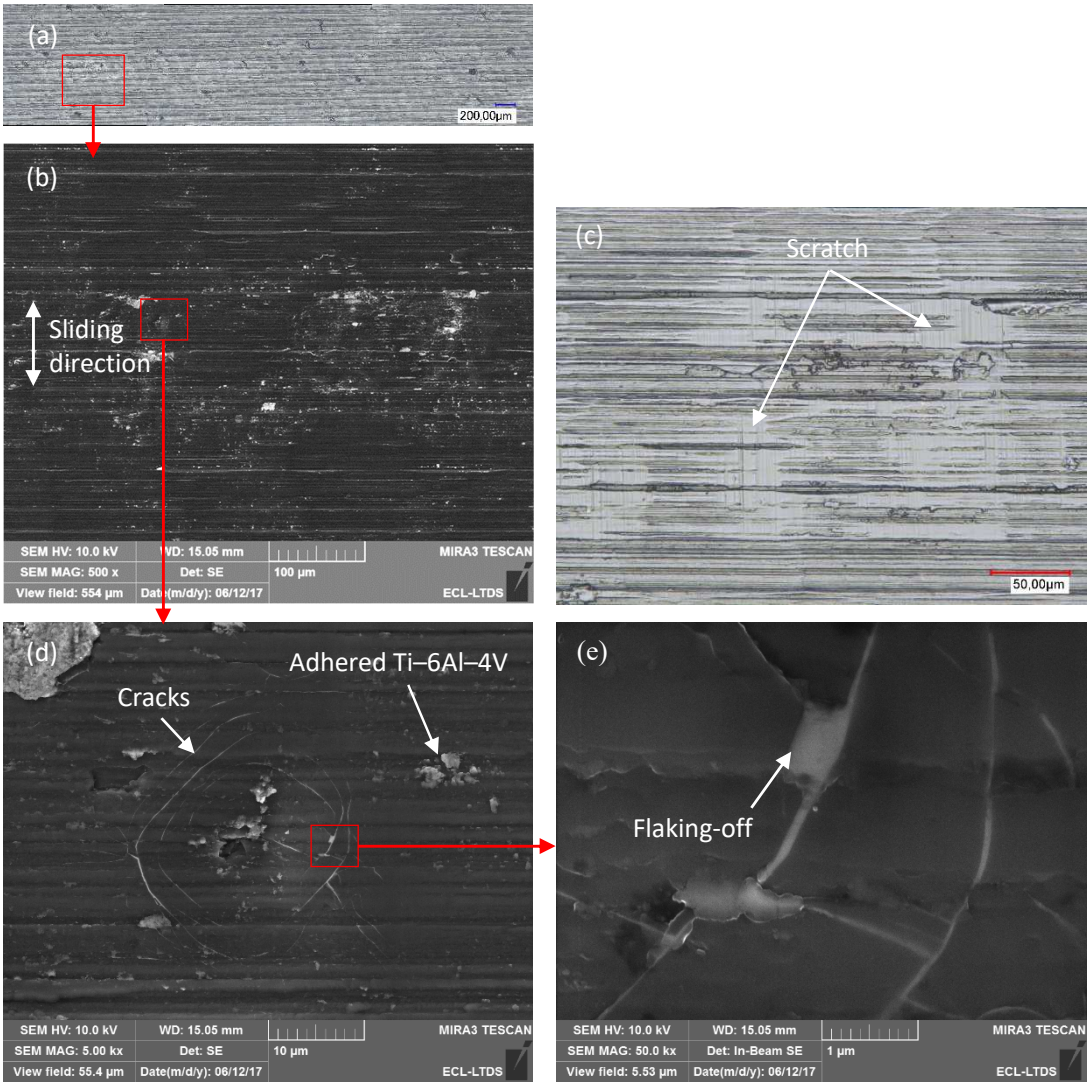
(a)
200,00µm
(b)
Sliding direction
SEM HV: 10.0 kV
WD: 15.05 mm
MIRA3 TESCAN
SEM MAG: 500 x
Det: SE
100 µm
View field: 554 µm
Date(m/d/y): 06/12/17
ECL-LTDS
(c)
Scratch
50,00µm
(d)
Cracks
Adhered Ti–6Al–4V
SEM HV: 10.0 kV
WD: 15.05 mm
MIRA3 TESCAN
SEM MAG: 5.00 kx
Det: SE
10 µm
View field: 55.4 µm
Date(m/d/y): 06/12/17
ECL-LTDS
(e)
Flaking-off
SEM HV: 10.0 kV
WD: 15.05 mm
MIRA3 TESCAN
SEM MAG: 50.0 kx
Det: In-Beam SE
1 µm
View field: 5.53 µm
Date(m/d/y): 06/12/17
ECL-LTDS

Fig. 24

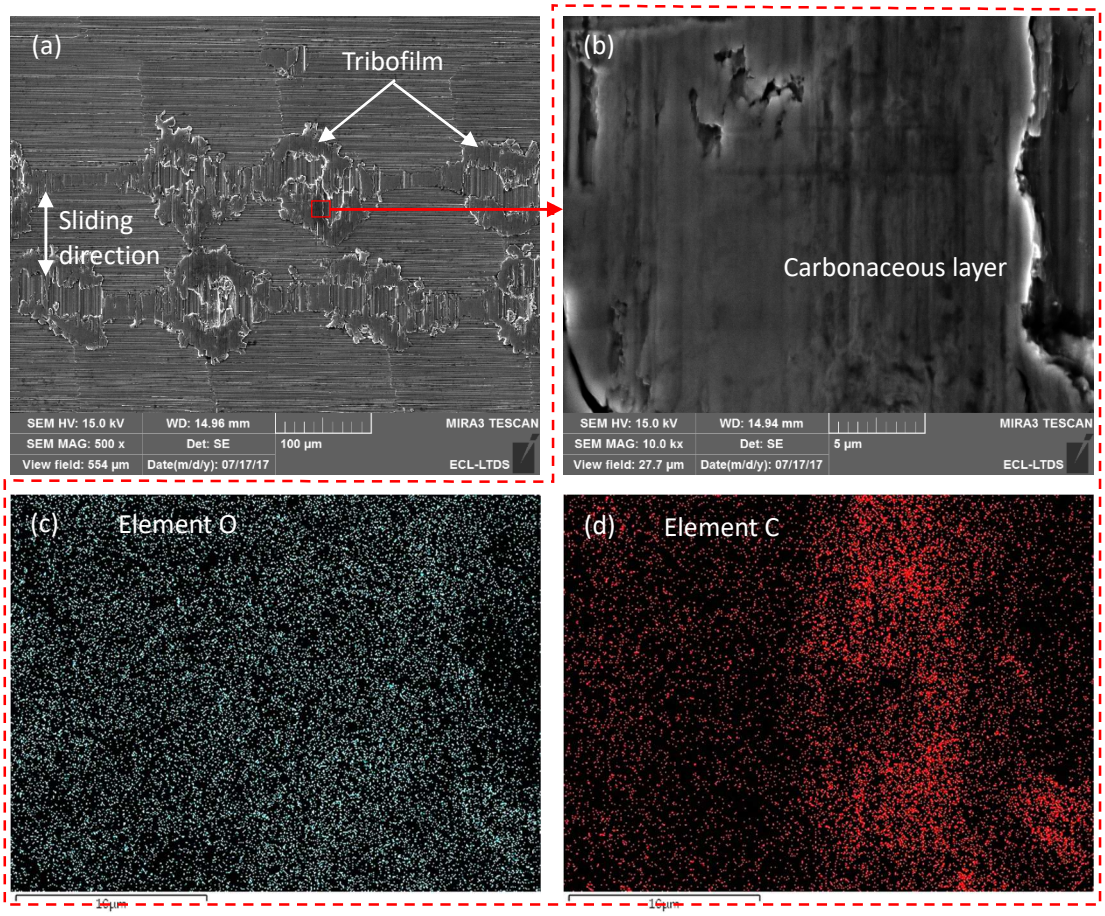
(a)
Tribofilm
Sliding direction
SEM HV: 15.0 kV
WD: 14.96 mm
MIRA3 TESCAN
SEM MAG: 500 x
Det: SE
100 µm
View field: 554 µm
Date(m/d/y): 07/17/17
ECL-LTDS
(b)
Carbonaceous layer
SEM HV: 15.0 kV
WD: 14.94 mm
MIRA3 TESCAN
SEM MAG: 10.0 kx
Det: SE
5 µm
View field: 27.7 µm
Date(m/d/y): 07/17/17
ECL-LTDS
(c)
Element O
(d)
Element C

Fig. 25

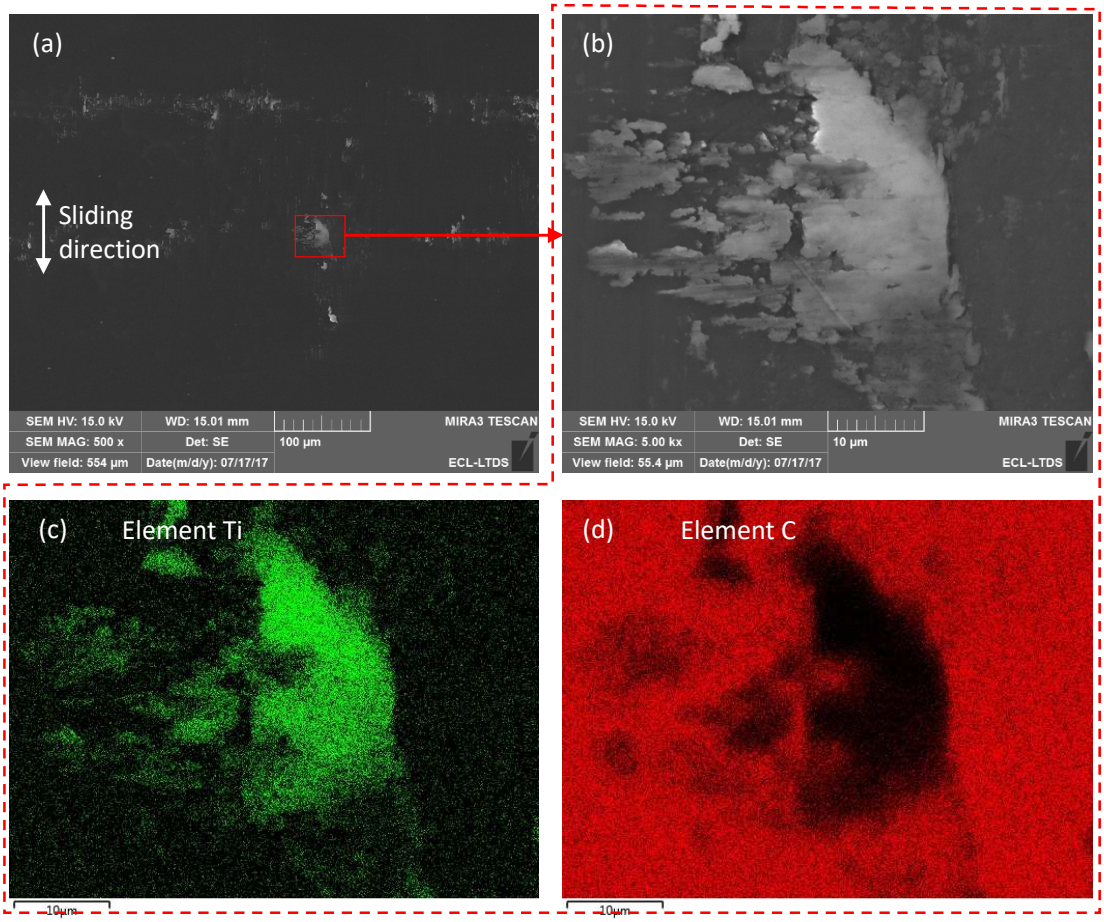
(a)
Sliding direction
SEM HV: 15.0 kV
WD: 15.01 mm
MIRA3 TESCAN
SEM MAG: 500 x
Det: SE
100 µm
View field: 554 µm
Date(m/d/y): 07/17/17
ECL-LTDS
(b)
SEM HV: 15.0 kV
WD: 15.01 mm
MIRA3 TESCAN
SEM MAG: 5.00 kx
Det: SE
10 µm
View field: 55.4 µm
Date(m/d/y): 07/17/17
ECL-LTDS
(c) Element Ti
10µm
(d) Element C
10µm

Fig. 26

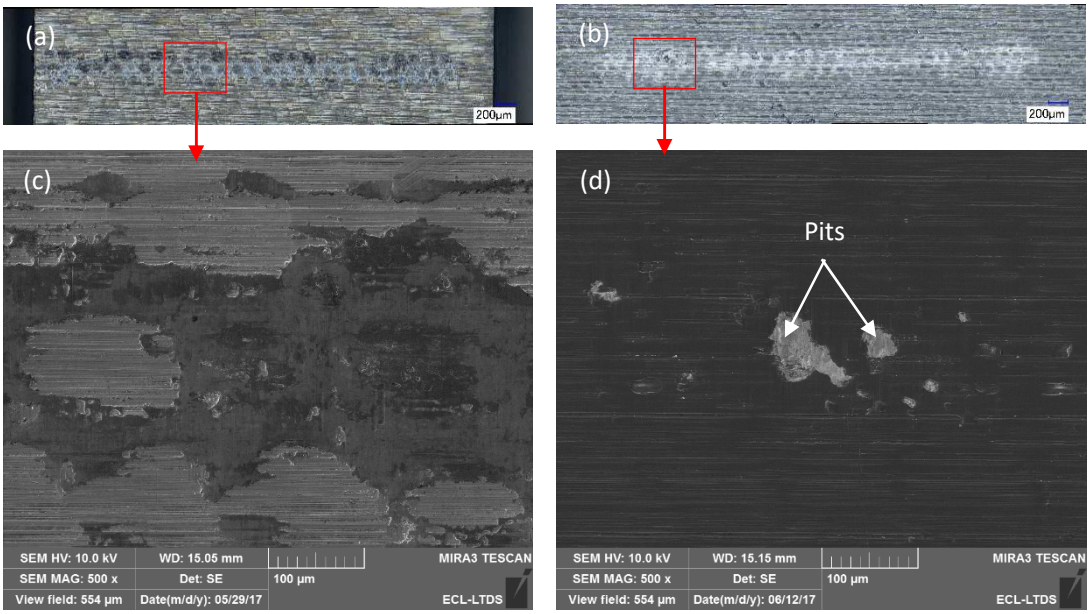
(a)
200µm
(b)
200µm
(c)
SEM HV: 10.0 kV
WD: 15.05 mm
MIRA3 TESCAN
SEM MAG: 500 x
Det: SE
100 µm
View field: 554 µm
Date(m/d/y): 05/29/17
ECL-LTDS
(d)
Pits
SEM HV: 10.0 kV
WD: 15.15 mm
MIRA3 TESCAN
SEM MAG: 500 x
Det: SE
100 µm
View field: 554 µm
Date(m/d/y): 06/12/17
ECL-LTDS

Fig. 27

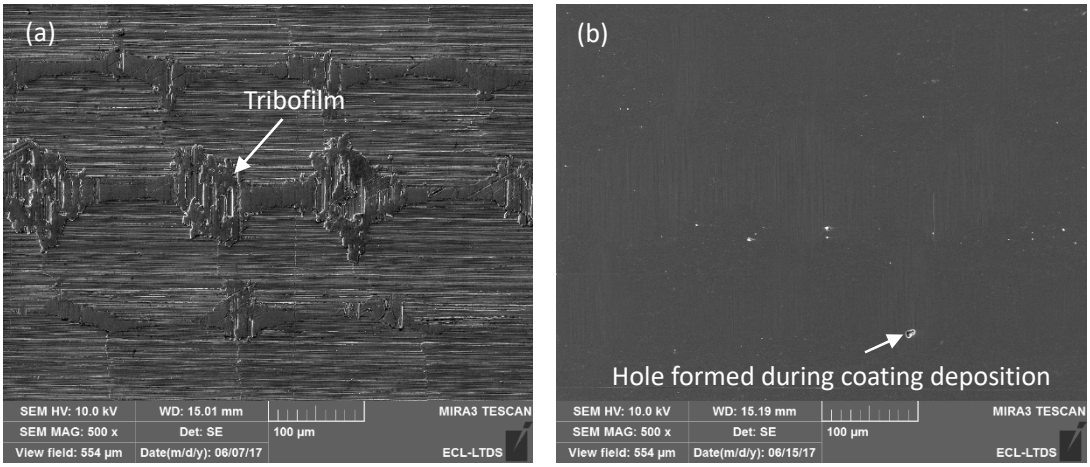
(a)
Tribofilm
SEM HV: 10.0 kV
WD: 15.01 mm
MIRA3 TESCAN
SEM MAG: 500 x
Det: SE
100 µm
View field: 554 µm
Date(m/d/y): 06/07/17
ECL-LTDS
(b)
Hole formed during coating deposition
SEM HV: 10.0 kV
WD: 15.19 mm
MIRA3 TESCAN
SEM MAG: 500 x
Det: SE
100 µm
View field: 554 µm
Date(m/d/y): 06/15/17
ECL-LTDS

Fig. 28

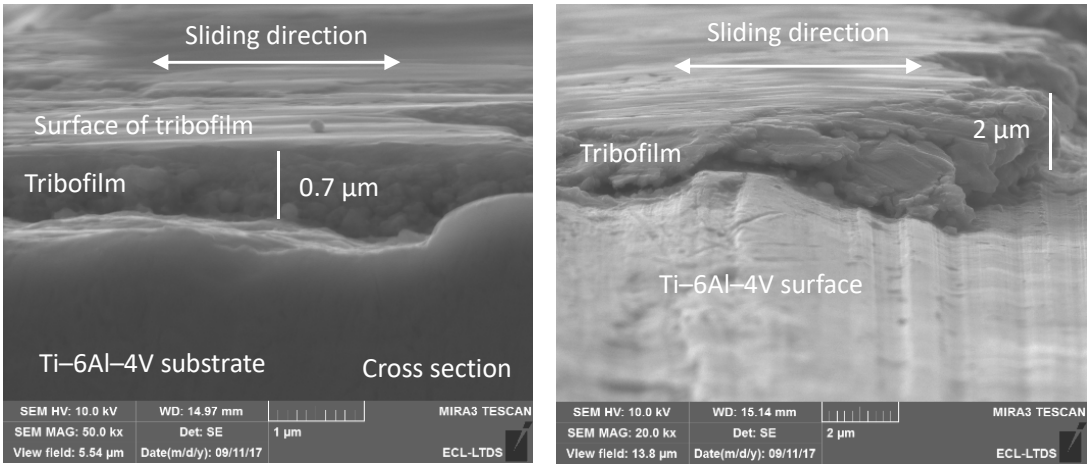
Sliding direction
Surface of tribofilm
Tribofilm
0.7 µm
Ti–6Al–4V substrate
Cross section
SEM HV: 10.0 kV
WD: 14.97 mm
MIRA3 TESCAN
SEM MAG: 50.0 kx
Det: SE
1 µm
Vlew field: 5.54 µm
Date(m/d/y): 09/11/17
ECL-LTDS
Sliding direction
2 µm
Tribofilm
Ti–6Al–4V surface
SEM HV: 10.0 kV
WD: 15.14 mm
MIRA3 TESCAN
SEM MAG: 20.0 kx
Det: SE
2 µm
Vlew field: 13.8 µm
Date(m/d/y): 09/11/17
ECL-LTDS

(a) (b)

Fig. 29

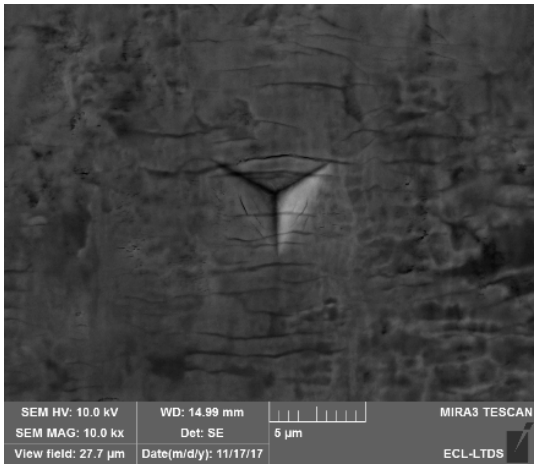
SEM HV: 10.0 kV
WD: 14.99 mm
MIRA3 TESCAN
SEM MAG: 10.0 kx
Det: SE
5 µm
View field: 27.7 µm
Date(m/d/y): 11/17/17
ECL-LTDS

(a)

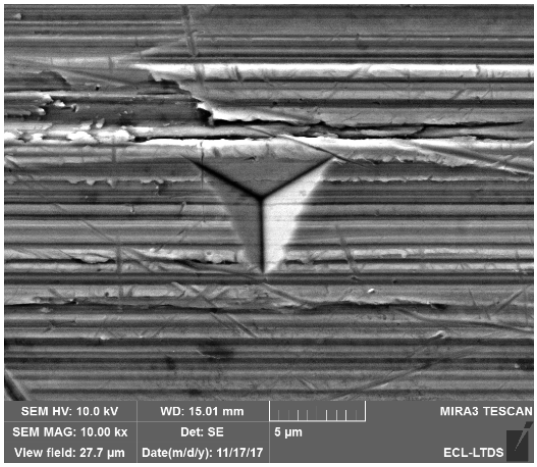
SEM HV: 10.0 kV
WD: 15.01 mm
MIRA3 TESCAN
SEM MAG: 10.00 kx
Det: SE
5 µm
View field: 27.7 µm
Date(m/d/y): 11/17/17
ECL-LTDS

(b)

Fig. 30

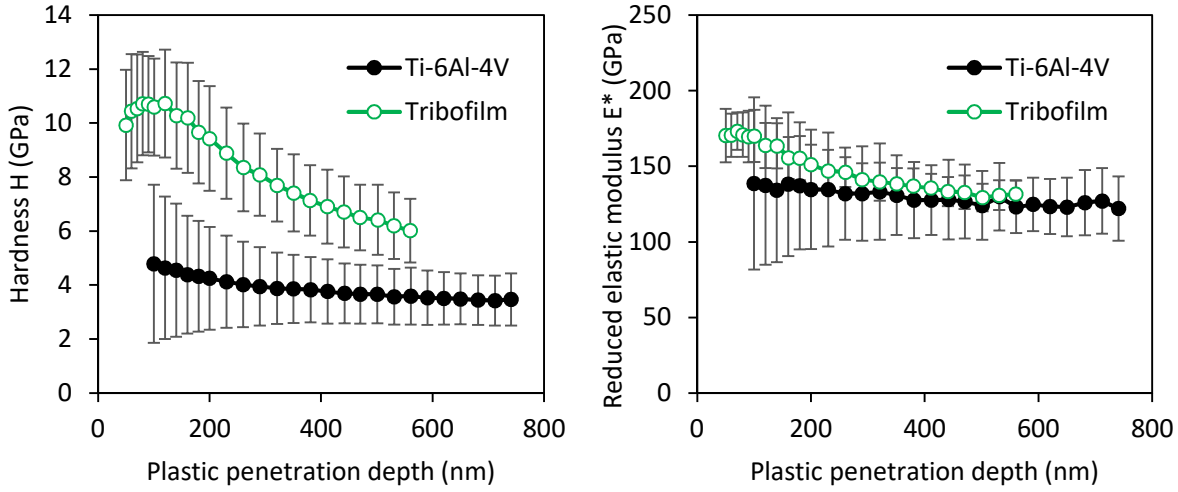
Hardness H (GPa)
Plastic penetration depth (nm)
Ti-6Al-4V
Tribofilm
Reduced elastic modulus E* (GPa)
Plastic penetration depth (nm)
Ti-6Al-4V
Tribofilm

(a) (b)

Fig. 31

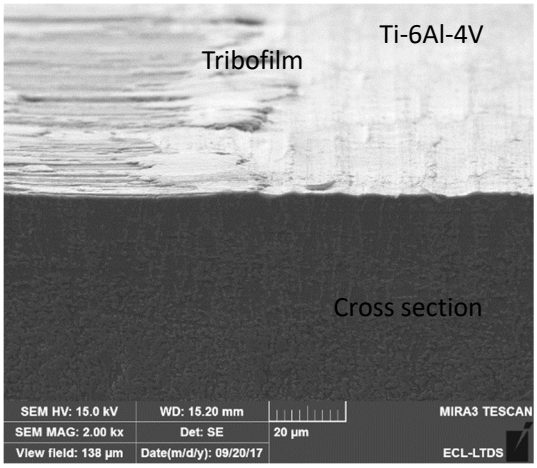
Ti-6Al-4V
Tribofilm
Cross section
SEM HV: 15.0 kV
WD: 15.20 mm
MIRA3 TESCAN
SEM MAG: 2.00 kx
Det: SE
20 µm
View field: 138 µm
Date(m/d/y): 09/20/17
ECL-LTDS

Fig .32

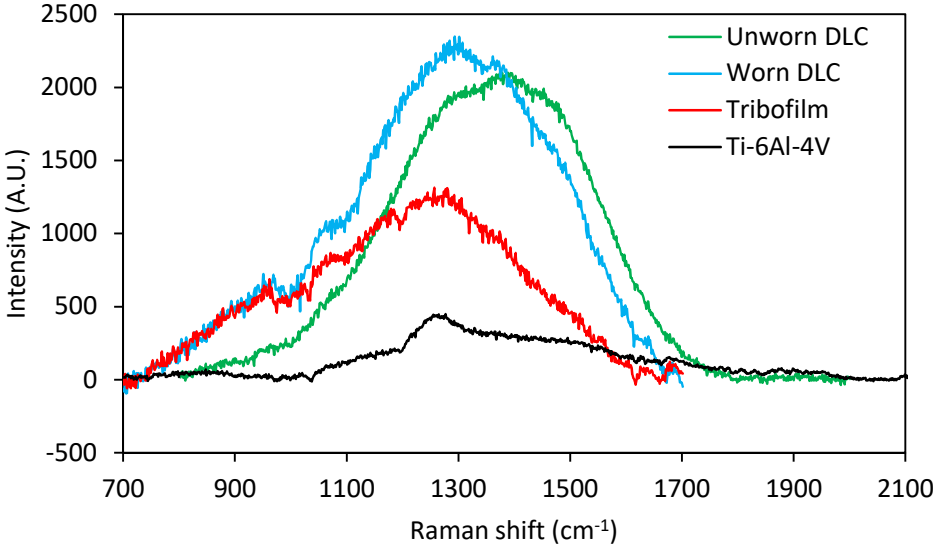
2500
2000
1500
1000
500
0
-500
Intensity (A.U.)
700
900
1100
1300
1500
1700
1900
2100
Raman shift (cm-1)
Unworn DLC
Worn DLC
Tribofilm
Ti-6Al-4V

Fig. 33

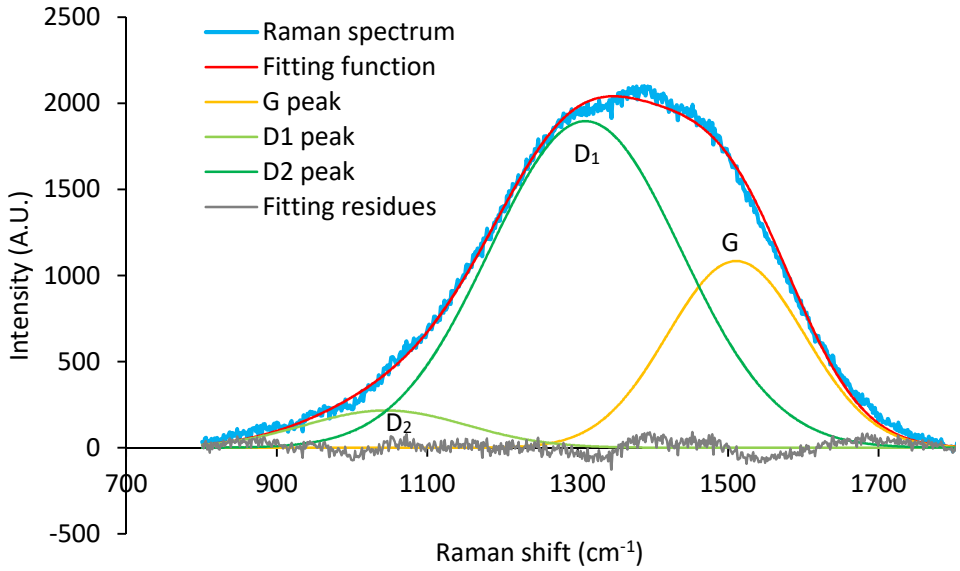
Raman spectrum
Fitting function
G peak
D1 peak
D2 peak
Fitting residues
Intensity (A.U.)
Raman shift (cm-1)
D1
G
D2
2500
2000
1500
1000
500
0
-500
700
900
1100
1300
1500
1700

(a)

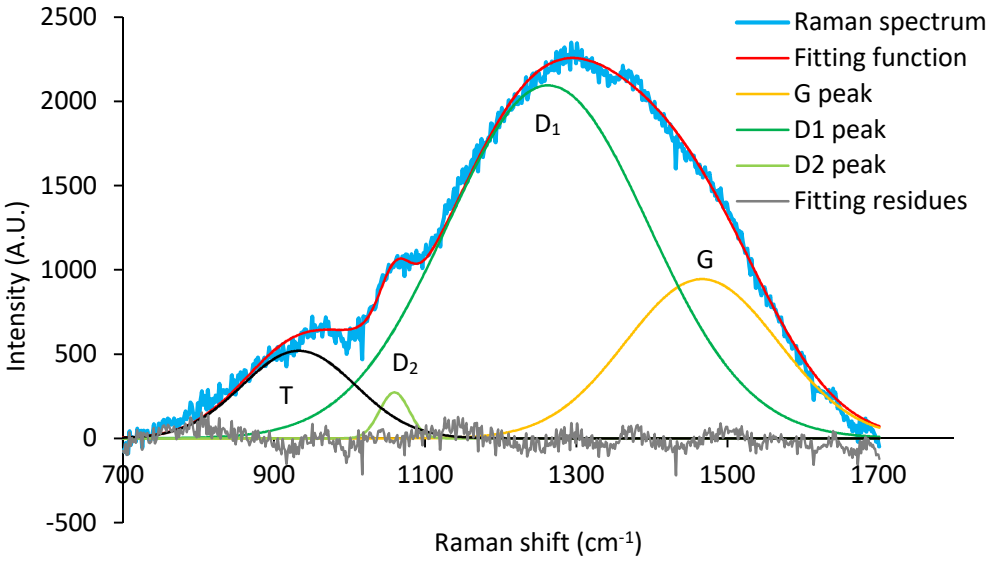
Raman spectrum
Fitting function
G peak
D1 peak
D2 peak
Fitting residues
Intensity (A.U.)
Raman shift (cm-1)
D1
G
D2
T
2500
2000
1500
1000
500
0
-500
700
900
1100
1300
1500
1700

(b)

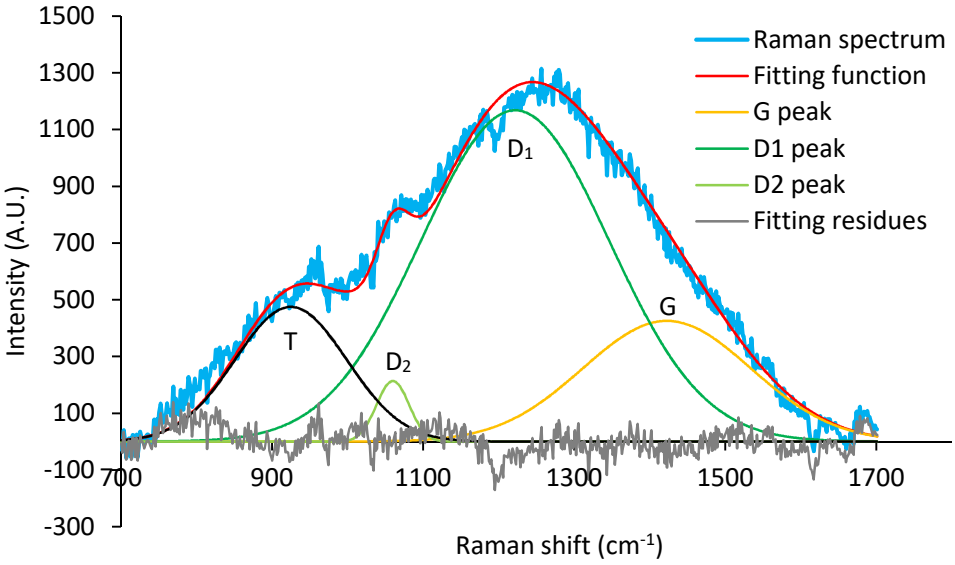
Raman spectrum
Fitting function
G peak
D1 peak
D2 peak
Fitting residues
Intensity (A.U.)
Raman shift (cm-1)
T
D2
D1
G
1500
1300
1100
900
700
500
300
100
-100
-300
700
900
1100
1300
1500
1700

(c)

Fig. 34

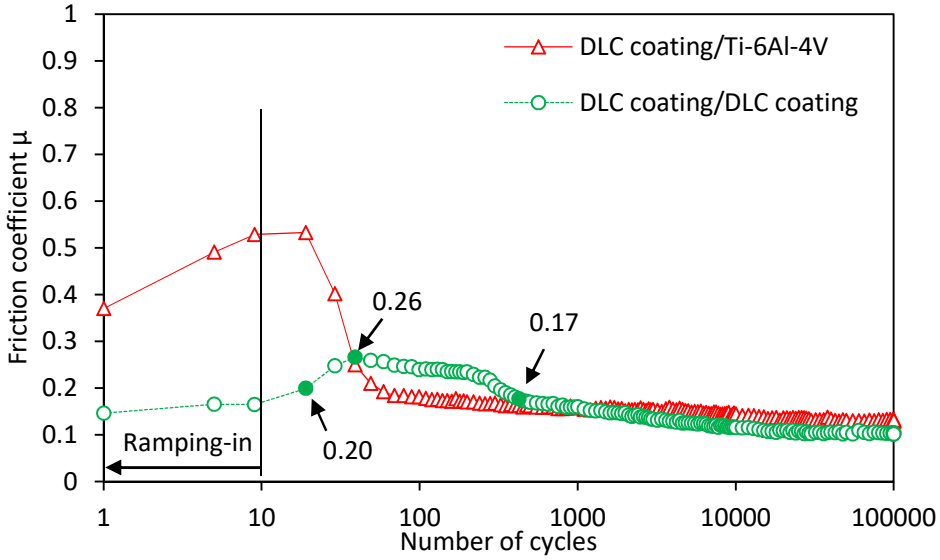
DLC coating/Ti-6Al-4V
DLC coating/DLC coating
Friction coefficient μ
Number of cycles
Ramping-in
0.26
0.17
0.20
1
0.9
0.8
0.7
0.6
0.5
0.4
0.3
0.2
0.1
0
1
10
100
1000
10000
100000

Fig. 35

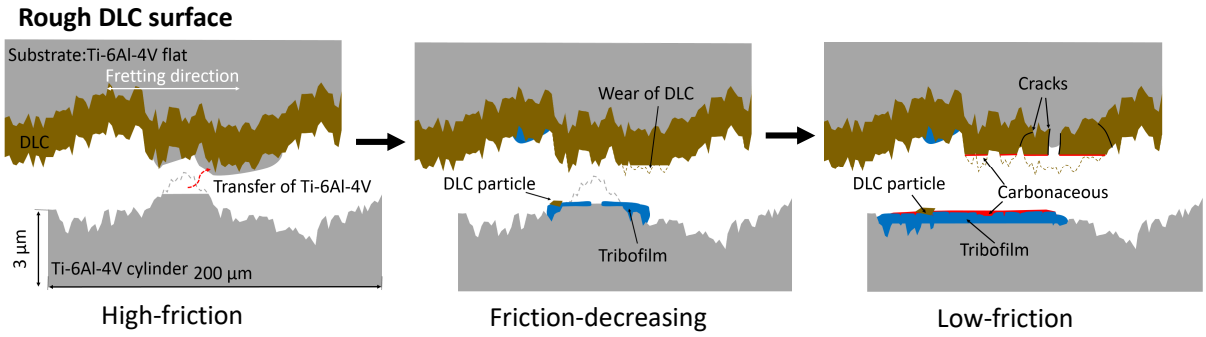
Rough DLC surface
Substrate:Ti-6Al-4V flat
Fretting direction
DLC
Transfer of Ti-6Al-4V
3 μm
Ti-6Al-4V cylinder 200 μm
High-friction
Wear of DLC
DLC particle
Tribofilm
Friction-decreasing
Cracks
DLC particle
Carbonaceous
Tribofilm
Low-friction

(a)

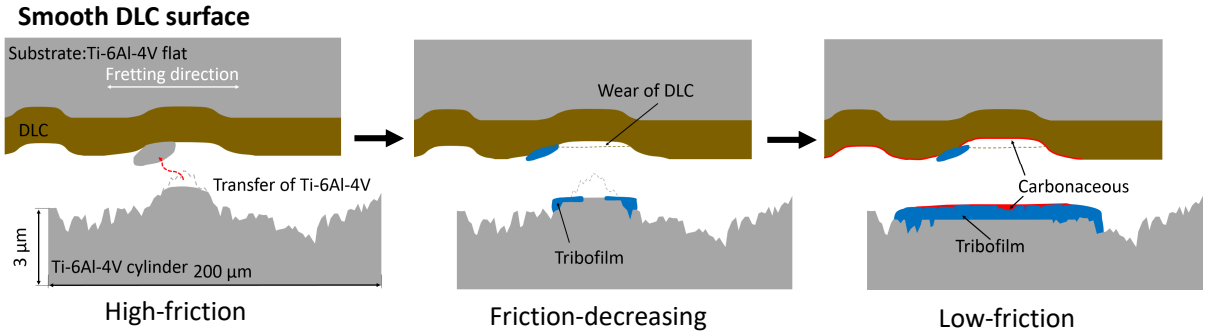
Smooth DLC surface
Substrate:Ti-6Al-4V flat
Fretting direction
DLC
Transfer of Ti-6Al-4V
3 μm
Ti-6Al-4V cylinder 200 μm
High-friction
Wear of DLC
Tribofilm
Friction-decreasing
Carbonaceous
Tribofilm
Low-friction

(b)

Captions of tables

Table 1

	DLC coating surface	Ti–6Al–4V countersurface	Friction during running-in
New test	New	New	High
Series 1	Rubbed	Rubbed	Low
Series 2	Rubbed	New	High
Series 3	New	Rubbed	Low

Table 2

		Unworn DLC	Worn DLC	Tribofilm
G peak	Position	1499 ± 13	1462 ± 16	1426 ± 10
	Intensity	1014 ± 77	1084 ± 301	382 ± 46
D_1 peak	Position	1307 ± 6	1258 ± 16	1221 ± 1
	Intensity	1823 ± 122	2323 ± 414	1085 ± 90
D_2 peak	Position	1056 ± 11	1057 ± 2	1061 ± 2
	Intensity	242 ± 31	309 ± 24	185 ± 26
$I(D_1+D_2)/I(G)$		2.04 ± 0.08	2.55 ± 0.67	3.33 ± 0.13

Table 3

No.	Flat	/	Cylinder	DLC coating surface	/	Countersurface	Friction
#1	New DLC	/	New Ti–6Al–4V	DLC	/	Ti–6Al–4V	High
#2	Rubbed DLC	/	Rubbed Ti–Al–4V	DLC + carbonaceous	/	Carbonaceous + tribofilm	Low
#3	Rubbed DLC	/	New Ti–6Al–4V	DLC + carbonaceous	/	Ti–6Al–4V	High
#4	New DLC	/	Rubbed Ti–6Al–4V	DLC	/	Carbonaceous + tribofilm	Low
#5	New DLC	/	New DLC	DLC	/	DLC	Low
#6	Rubbed DLC	/	Rubbed DLC	DLC + carbonaceous	/	Carbonaceous + DLC	Low